Supplementary Information

High-efficiency atmospheric water harvesting enabled by ultrasonic extraction

Ikra Iftekhar Shuvo[1,2], Carlos D. Díaz-Marín[2], Marvin Christen[3], Michael Lherbette[3], Christopher Liem[4], Svetlana V. Boriskina[2,*]

[1]Media Lab, Massachusetts Institute of Technology, Cambridge, MA 02139, USA
[2]Department of Mechanical Engineering, Massachusetts Institute of Technology, Cambridge, MA 02139, USA
[3]SmarAct Metrology GmbH & Co. KG, Oldenburg, HRA 207391, Germany.
[4]Department of Electrical Engineering and Computer Science, Massachusetts Institute of Technology, Cambridge, MA 02139, USA

*Corresponding author: sborisk@mit.edu

1. Supplementary Notes

1.1. Supplementary Note 1 - Piezoelectricity and constitutive piezoelectric equations

In our study, we utilized the converse piezoelectric effect (i.e., mechanical deformations of the material caused by the applied electric field) of an ultrasound transducer to operate it as an actuator to remove water from a hydrogel. We also proposed to utilize a direct piezoelectric effect (i.e., electrical charge generation under mechanical pressure) as a mechanism of in-situ monitoring and control of the moisture harvesting and extraction processes. Supplementary Fig. S1 schematically illustrates the piezoelectric and converse piezoelectric phenomena[1].

The fundamental interactions between the electrical and mechanical characteristics of piezoelectric materials and the surrounding environment are characterized by two constitutive piezoelectric equations, commonly known as the actuator and sensor equations[1,2] (Eq. S1):

$$\begin{bmatrix} S \\ D \end{bmatrix} = \begin{bmatrix} s^E & d \\ d & \varepsilon \end{bmatrix} \begin{bmatrix} T \\ E \end{bmatrix}. \quad \text{(S1)}$$

Actuator equation:

$$S = du/dx = s^E T + dE. \quad \text{(S2)}$$

Sensor equation:

$$D = dT + \varepsilon E. \quad \text{(S3)}$$

Here,

D is the dielectric (charge density) displacement
$S = du/dx$ is the induced strain
E is the electric field
s^E is an elastic compliance at constant electric field
T is stress
E is the dielectric permittivity at constant temperature
d is a piezoelectric strain constant

1.2 Supplementary Note 2 - Numerical analysis using multi-physics modelling technique

PZT polycrystal was used in this study to make the actuating devices. It is a widely used commercial piezoelectric materials due to its high energy conversion rate and piezoelectric coefficients[1]. The strain-charge relationship for a PZT material could be expressed as[3]:

$$\begin{bmatrix} S_1 \\ S_2 \\ S_3 \\ S_4 \\ S_5 \\ S_6 \end{bmatrix} = \begin{bmatrix} s_{11}^E & s_{12}^E & s_{13}^E & 0 & 0 & 0 \\ s_{21}^E & s_{22}^E & s_{23}^E & 0 & 0 & 0 \\ s_{31}^E & s_{32}^E & s_{33}^E & 0 & 0 & 0 \\ 0 & 0 & 0 & s_{44}^E & 0 & 0 \\ 0 & 0 & 0 & 0 & s_{55}^E & 0 \\ 0 & 0 & 0 & 0 & 0 & s_{66}^E = 2(s_{11}^E - s_{12}^E) \end{bmatrix} \begin{bmatrix} T_1 \\ T_2 \\ T_3 \\ T_4 \\ T_5 \\ T_6 \end{bmatrix} + \begin{bmatrix} 0 & 0 & d_{31} \\ 0 & 0 & d_{32} \\ 0 & 0 & d_{33} \\ 0 & d_{24} & 0 \\ d_{15} & 0 & 0 \\ 0 & 0 & 0 \end{bmatrix} \begin{bmatrix} E_1 \\ E_2 \\ E_3 \end{bmatrix} \quad \text{(S4)}$$

$$\begin{bmatrix} D_1 \\ D_2 \\ D_3 \end{bmatrix} = \begin{bmatrix} 0 & 0 & 0 & 0 & d_{15} & 0 \\ 0 & 0 & 0 & d_{24} & 0 & 0 \\ d_{31} & d_{32} & d_{33} & 0 & 0 & 0 \end{bmatrix} \begin{bmatrix} T_1 \\ T_2 \\ T_3 \\ T_4 \\ T_5 \\ T_6 \end{bmatrix} + \begin{bmatrix} \varepsilon_{11} & 0 & 0 \\ 0 & \varepsilon_{22} & 0 \\ 0 & 0 & \varepsilon_{33} \end{bmatrix} \begin{bmatrix} E_1 \\ E_2 \\ E_3 \end{bmatrix}. \quad \text{(S5)}$$

Piezoelectric strain coefficient matrix for the PZT polycrystal has the following form[4]:

$$[d_{ij}] = \begin{bmatrix} 0 & 0 & d_{31} \\ 0 & 0 & d_{32} \\ 0 & 0 & d_{33} \\ 0 & d_{24} & 0 \\ d_{15} & 0 & 0 \\ 0 & 0 & 0 \end{bmatrix}. \quad \text{(S6)}$$

The governing equations of piezoelectricity used to calculate the vibrational modes of the actuating membrane and the acoustic wave propagation through hydrogel samples include the momentum equation (Newton's second law, Eq. S7) and the charge conservation equation (Eq. S8):

$$\rho \frac{d^2 \boldsymbol{u}}{dt^2} = \nabla \cdot S + \boldsymbol{F}, \quad \text{(S7)}$$

$$\nabla \cdot \boldsymbol{D} = \rho_V, \quad \text{(S8)}$$

where ρ_V is a volume charge density, ρ is a solid density, $\boldsymbol{u}$ is a solid displacement vector, $\boldsymbol{F}$ if the force per unit volume.

The electric field is computed from the electric potential V:

$$E = -\nabla V. \quad \text{(S9)}$$

COMSOL Multiphysics (6.1) was used to calculate vibrational eigenfrequencies and the associated eigenmodes[5] of a piezo actuator driven by sinusoidal voltage.

1.3. Supplementary Note 3 – FTIR analysis of hydrogels

We used the Fourier-transform infrared spectroscopy (FTIR) to reveal the changes in the hydrogen properties underlying ultrasonic-driven water extraction in process (see Methods). PAM hydrogels contains major functional groups like methylene (-CH_2-), carbonyl (C=O) and amino group (-NH_2), which form hydrogen (H-) bonds with H_2O and may play a crucial role in the configuration of adsorbed water molecules[6]. The interplay of heat and kinetic pressure induced by ultrasonic actuation breaks some of these hydrogen bonds, facilitating water extraction. The resulting reduced moisture content is manifested by the shifts and intensity changes of the peaks in the FTIR spectra of hydrogels[7,8].

Supplementary Fig. S26 compares the FTIR spectra of (i) as-prepared (pristine) hydrogels (HG-A and HG-C), (ii) hydrogels after 30 minutes of ultrasound actuation (US 30 min), (iii) hydrogels exposed to the environment with 25% RH for 30 minutes at 21^{o}C following US actuation (Abs. 30 min), and (iv) pure DI water. Two broad absorptance bands observed in the FTIR spectra of HG-A and HG-C hydrogels between 2800 cm^{-1} and 3800 cm^{-1} and between 1500 and 1800 cm^{-1} in Supplementary Figs. S26a and S26e, respectively, have been deconvoluted into individual Gaussian peaks corresponding to different vibrational modes of the polymer functional groups and water molecules[7–9] (Supplementary Figs. S26b-d,f-h, see Methods). Several peaks have been fitted and assigned to different vibrational modes based on prior literature data (see Supplementary Table 2.3)[9].

These data reveal that the water content in the sorbent material, which is varied under the piezoelectric actuation and moisture adsorption process, is manifested in the changes in vibrational peak positions and relative intensities. A more detailed analysis of FTIR spectra of different sorbents under different harvesting and ultrasonic actuation scenarios is expected to offer valuable insights into the molecular dynamics of the polymer chains and their interactions with water molecules. Such an analysis will be a subject of a separate study focused on the development of optimized ultrasound-responsive water harvesting hydrogels with thermodynamics-limit-breaking energy efficiency moisture extraction performance.

1.4. Supplementary Note 4 – Efficiency calculation of the device

The efficiency of the water release process, η, was calculated as [10,11]:

$$\eta = \frac{h_{lv}}{E} \times 100\% \quad \text{(S10)}$$

where $h_{lv} = 2.257\ [\mathrm{MJ/kg}]$ is the enthalpy of vaporization of water and $E\ [\mathrm{MJ/kg}]$ is the specific energy consumption defined as the energy input (electrical, thermal, or a combination thereof, depending on each individual system configuration) divided by the mass of water released from a sorbent. In an ideal thermal process, all the heat provided to the system is used to evaporate water

i.e., $E = h_{lv}$, where it is also considered that the enthalpy of desorption is identical to the enthalpy of vaporization of water. Therefore, an ideal thermal process has $\eta = 100\%$. In this work, we refer to this ideal thermal process with $\eta = 100\%$ as the thermal limit. In a real thermal water release process, the heat provided is used not only evaporate water, but also to sensibly heat the system and sorbent, and is partially lost to the ambient, leading to $\eta < 100\%$.

For our experiments, the energy consumption (E) after the weight-loss experiment was calculated using the following equation, where P is input energy, m is the output extracted weight or amount of weight loss measured in g, and $1\ Wh = 3.6 \cdot 10^3\ J$:

$$E\left[\frac{MJ}{kg}\right] = \frac{P}{m} = \frac{\text{Supplied power } [MJ]}{m\ [kg]}$$
$$= \frac{V[V] \cdot I[A] \cdot \text{Actuation time } [h] \cdot \text{Duty cycle} \cdot 3.6\left[\frac{J}{Wh}\right] \cdot 10^3}{m\ [g] \cdot 10^{-3}}$$

As an example, when we applied 5 V and 0.3 A at 70% duty cycle for 10 min (~0.17 hr) using our piezoelectric actuator to desorb water from HG-M (Fig. 4E), the weight loss was measured to be 0.13 ± 0.002 g. Then, the energy consumption per unit mass of water extracted can be calculated as:

$$E = \frac{5[V] \cdot 0.3[A] \cdot 0.17\ [h] \cdot 0.7 \cdot 3.6\left[\frac{J}{Wh}\right] \cdot 10^3}{0.13\ [g] \cdot 10^{-3}} = 4.84\left[\frac{MJ}{kg}\right] = 1.35\ \left[\frac{kWh}{kg}\right]$$

Then, the efficiency of the water release process, η, can be calculated as:

$$\eta = \frac{h_{lv}}{E} \times 100\% = \frac{2.25\left[\frac{MJ}{kg}\right]}{4.84\ \left[\frac{MJ}{kg}\right]} \times 100\% = \sim 46.4\%$$

Note that this is the device-level energy efficiency, which explicitly captures all the energy losses during the extraction system operation. In the manuscript, we demonstrate that this efficiency depends on the actuation time and decreases during longer actuation periods. Cycling testing of the system under different actuation periods revealed that short actuation times (2 minutes) yield the highest extraction energy efficiency and even allow energy consumption lower than the thermal limit.

We compared our results with the specific energy consumption E and moisture extraction energy efficiency η data for several experimentally demonstrated atmospheric water harvesting

systems[10]. These values are summarized in Table 4, which is shown below. The table also shows the estimates of the moisture extraction efficiency per unit mass per day. Note that, unlike the specific energy consumption E and extracted water mass m, the daily values E_d and m_d are either measured over a daily collection/extraction cycle or estimated by accounting the time needed to collect the moisture from the atmosphere before it can be extracted. All the values in the table represent the experimentally obtained system-level performance data in a daily harvesting cycle and, as such, can be compared on equal footing.

Note that under the above standard definition of the efficiency (η) of AWH systems, an efficient non-thermal extraction method can have a specific energy consumption lower than the enthalpy of vaporization of water, h_{lv}. In this case, the energy efficiency of the water release process can exceed 100%. This is the case measured and reported in our manuscript, which we describe as 'breaking the thermal limit.

1.5. Supplementary Note 5 – Scaled-up AWH system performance estimate

To evaluate the daily water yield and energy efficiency of extraction for an AWH device scaled to the 1-m^2 area, we implemented the simplest scale-up strategy, which assumes that multiple identical actuators with hydrogel samples identical to those used in our study will be deployed in the form of a 2D array with the total area of the sample surface equal to 1 m^2. We further assume that each actuator will be powered separately and the energy consumption per device will be the same as measured in our experiments. This is likely not the most efficient way of scaling the system up and would overestimate the daily energy consumption of the system and underestimate the energy efficiency of extraction.

To illustrate the validity of the simple scaling-up approach, we first performed a test using three identical actuators simultaneously (Figs. S33-S34). Three hydrogel samples weighing about 2.6g, after sorption at 75% relative humidity, were simultaneously stimulated by three piezoelectric ultrasonic devices operating at a 25% duty cycle for 10-min. In all cases, the specimens exhibited a loss above 0.1 g. The measured specific energy consumption ranged from 1.9 to 2.1 MJ/kg after 2-min and from 4.2 to 5.8 MJ/kg after 10-min actuation (Fig. S34), comparable to the same values measured in a single-actuator device shown in Table S4.

The daily yield of water from a 1-m^2 sorbent area [L/m^2/day] has been calculated by extrapolating the results of cyclic sorption-desorption testing of a single prototype device over 10 hours at 75% RH. The piezo actuator has a surface area of 0.0002 m^2 (diameter = 16mm), and the sorbent has a surface area of 0.0009 m^2 (diameter = 34 mm).

Fig. 6a shows the extracted water mass and energy efficiency for each extraction cycle (with ten 1-hour-long sorption cycles separated by eleven 2-minute-long extraction cycles). During each 2-

minute-long extraction cycle, energy consumption was recorded to be below the enthalpy of water vaporization, thus yielding extraction efficiency in excess of 100%.

To estimate the water yield per device per day, we first calculated the average sorption and desorption rates by using the data shown in Fig. 6a. The average collection and extraction rate is around 0.13 g/hr and 0.08 g/2min. The extraction rate exceeds the collection rate by a factor of ~18.5, and during a 1-hr harvesting period, the sorbent collects more water than can be extracted in 2 min. These data indicate that to maximize and balance both the sorption and desorption processes over the course of one day, the system may be operated in 34 sorption-extraction cycles per 24 hours, each cycle comprised of about 40 minutes of collection followed by 2 minutes of extraction (see Table S5). Under this operational scenario, all the harvested moisture will be extracted with low energy expenditure, as it takes about 2 minutes to extract the whole amount of moisture harvested over 40 minutes at 75%RH. For operation at RH different than 75%, a different sorption-desorption cycle ratio may need to be implemented, to be optimized separately for each RH level.

To extrapolate the water yield to a 1-m^2 sorbent area, this number was further scaled up from one device having 0.0009-m^2 sorbent area to a 1-m^2-area array. The resulting average daily productivity value has been predicted to be ~3.2 [$L/m^2/day$]. Note that with our approach, harvesting can be done during both night and day (unlike the devices relying on solar-driven evaporation). In turn, the device efficiency of 0.16 kWh/kg (0.576 MJ/kg) was calculated by using the average mass extracted from each of two hydrogel specimens over eleven 2-min-long extraction cycles (see Table S5).

Fig. 6b illustrates an alternative method of device operation, consisting of continuous harvesting for 24 hours at 75%RH, followed by desorption involving 25 consecutive cycles of 2-minute-long extractions over a total duration of 50 minutes (i.e., without a sorption period in between the cycles), resulting in the desorption of 1g of water at an energy cost of 1.13 MJ/kg. This energy expenditure is nearly a factor of two greater than the average energy cost observed for the 2-minute-long extraction cycles depicted in Fig. 6a.

These methods together demonstrate the adaptability of our system, which is not constrained by temporal limitations, unlike the solar-derived desorption mechanism that operates based on the availability of sufficient or proper daylight hours at a slower desorption rate in comparison to our system. We chose the lower-energy-expenditure approach illustrated in Fig. 6a to estimate the daily yield and the cost of the harvested water.

We conducted similar studies with smaller specimens (≤16 mm diameter) and observed similar cyclic stability and energy efficiency as shown in Fig. S35. It can be seen that in this case the collection rate is much slower than the extraction rate, and during a 1-hr harvesting period, the sorbent collects less water than can be extracted in 2 minutes of actuation (see Table S6). As such, harvesting time imposes the upper limit on the daily water yield.

In this case, to balance the mass of harvested and extracted water over a 24-hour cycle, we assume 12 sorption-extraction cycles per 24 hours, each comprised of ~ 2 hours (118 min) of collection followed by ~2-minutes of extraction. During 118 min of collection, slightly less water is absorbed per device than can be extracted in 2 minutes, so we assume that each extraction period will be slightly less than 2 minutes long. The average daily water yield per device at 75%RH is calculated as the amount of water collected over twelve 118-min-long cycles. To extrapolate the water yield to a 1 m^2 sorbent area, this number was further scaled up from one device area to 1 m^2. The resulting average daily productivity value has been predicted to be ~1.5 [L/m^2/day], and the average energy consumption - 0.411 kWh/kg (1.48 MJ/kg).

1.6. Supplementary Note 6 – Ideal limit of moisture extraction from air by dewing

The minimum energy intensity per unit mass of water $\frac{Q_{in}}{m_w}$ required for dewing can be calculated as follows:

$$\frac{Q_{in}}{m_w} = \left[\frac{1}{\omega_i}(c_{p,air} + \omega_0 c_{p,v})(T_0 - T_r) + h_{fg}\right] COP^{-1},$$

where ω_0 is the ambient humidity, $c_{p,air}$ and $c_{p,v}$ are the specific heat capacity of air and vapor, respectively, T_r is the dewpoint temperature, and h_{fg} is the enthalpy of vaporization of water at T_0, equivalent to the latent heat removed during condensation. The term $\frac{1}{\omega_i}(c_{p,air} + \omega_i c_{p,v})(T_0 - T_r)$ represents the sensible heat removed from the air and moisture to cool it down to the dew point temperature. COP is the coefficient of performance of the refrigerator used to remove heat. For an ideal refrigerator, $COP = \frac{T_r}{T_0 - T_r}$.

At $\omega_0 = 75\%\ RH$ and $T_0 = 25°C$, the minimum energy required for dewing is 0.58 MJ/kg (0.16 kWh/kg). This is the ideal dewing limit (corresponding to $COP = 4.32$).

Actual dehumidifying systems typically operate at COP values between 3 and 4, which will increase the energy intensity to 0.23 kWh/kg or 0.173kWh/kg, respectively. As an example, whole-home dehumidifiers with a volume of 8.0 ft^3 or less are certified by the U.S. Department of Energy (DOE) to be ENERGY STAR-level efficient if they operate at 0.48 kWh/kg energy intensity (i.e., have an Integrated Energy Factor IEF=2.09 L/kWh). Dehumidifiers with a volume over 8.0 ft^3 are certified as ENERGY STAR-level efficient if they operate at 0.303 kWh/kg energy intensity (IEF=3.3 L/kWh).

1.7. Supplementary Note 7 – Preliminary techno-economic analysis

By modifying the technoeconomic feasibility study conducted by Zhong et al.[11] on sorption-based atmospheric water harvesting (SAWH) system, we carried out a preliminary technoeconomic analysis of our system. Contrary to that study, we consider that the lifespan of the material and device are distinct. In addition, we included the cost of supplied electric power into cost of water production (Cost of water, in units of $/L), which is calculated as:

$$Cost\ of\ water = \ Capital\ expenditure\ (CAPEX) + \ Operational\ expenditure\ (OPEX)$$

$$= \frac{\left(\frac{(Cost_{hydrogel} \cdot \rho_{hydrogel} \cdot V_{hydrogel}}{\tau_{hydrogel}} + \frac{Cost_{device}}{\tau_{device}}\right)}{Yield} \ + \ (Electricity\ cost \cdot Energy\ intensity)$$

Here,

$Cost_{hydrogel}$ = cost of hydrogel-salt composite per kg of material in the dry state,

$\rho_{hydrogel}$ = density (2000 kg/m^3)[12] of the hydrogel-salt composite in the dry state,

$V_{hydrogel} = A_{hydrogel} \cdot H_{hydrogel}$ = volume of the hydrogel-salt composite in the dry state,

$A_{hydrogel} = 1$ m^2 area of the hydrogel-salt composite, making cost per m^2 of our overall system,

$H_{hydrogel}$ = typical hydrogel-salt composite thicknesses used in our device ~1mm (=0.001m),

$\tau_{hydrogel}$ = hydrogel lifetime in days (30-365 days), which is one of the variables of analysis,

$Cost_{device}$ = cost of the SAWH device excluding the sorbent cost,

τ_{device} = lifetime of the piezoelectric PZT actuator (20-45 years), which is another variable [13,14],

$Yield\ or\ productivity$ = amount of water produced by day (L/m^2/day),

$Electricity\ cost$ = 0.17 $/kWh, electricity price based on US Bureau of Labor Statistics [15],

$Energy\ intensity$ = supplied energy per liter of desorbed water, expressed in kWh/L

Supplementary Table 8 summarizes all the costs of the hydrogel-salt composite ingredients and an actuator unit as well as the energy cost of operating the actuator. With these data, we estimate the $Cost_{hydrogel}$ and $Cost_{device}$ are 0.4-1.1 $/kg and 1111-2222 $/m^2 (based on a single device used for a gel with 34 mm diameter), respectively.

The daily yield of water of 3.25 kg/m^2/day has been estimated from the results of the cyclic sorption/extraction experiment as detailed in Supplementary Note 5 above. CAPEX, OPEX, and cost of water were then estimated to be 0.05-0.09 $/L, 0.1 $/L, and 0.19 $/L (Fig. S36) assuming the device lifespan of 25 years and hydrogel lifespan of 30 days (Fig. S37). Based on a worldwide survey conducted on 2023, the cost of a fresh bottled water, ranges between 0.23 and 1.35 $/L around the globe as shown in Fig. S37, and thereby, estimated to have an average price of 0.79 $/L (data taken from [16]).

1.8. Supplementary Note 8 – Structural integrity of hydrogel under ultrasonic extraction

To evaluate the structural integrity of the hydrogel and the extracted water quality after desorption, the water extracted from LiCl-PAM hydrogels (HG-A) were filtered using a VWR@ sterile syringe filter, commonly employed for ICP-OES testing. In this experiment, three piezoelectric devices were used to extract water from a ~5.92 g HG-A specimen at a duty cycle of 25-30% over a duration of ~45 min. The setup and test were made and conducted within an enclosed petri dish, respectively. Following desorption, ~0.21 ml of desorbed water was collected from the petri dish lid and subsequently filtered using a VWR filter paper kit to examine for any traces of polymer residue.

The initial dry weight of the filter paper kit was ~2.99 g, which increased to ~3.02 g after the filtration of ~0.21 ml extracted water at 20% relative humidity, resulting in wetting the filter paper. Following drying at room temperature, the weight of the filter paper returned to 2.99 g, with no polymer residue detected. This provides the evidence that hydrogels remained intact following the ultrasonic actuation process, and the extracted water is not contaminated by the polymer.

1.9. Supplementary Note 9 – Li content in the water extracted from LiCl-PAM hydrogels

We additionally analyzed Li content in the water extracted from LiCl-PAM hydrogels. There are no regulatory thresholds for lithium either in the USA or globally, and EPA doesn't have a specific health advisory for lithium in a drinking water [17,18]. While typical therapeutic oral doses of Li are as high as 600–1200 mg/day [19], Li may pose a potential concern for human health, and some studies recommend to limit casual Li-ion intake to 3.1 mg per day[20]. At the same time, recent studies of bottled water from dozens of countries revealed a wide range of Li content, from ~0 to 9.9 mg/L [18,21].

We conducted the inductively coupled plasma optical emission spectrometer (ICP-OES) elemental analysis on the water desorbed from a LiCl-PAM hydrogel to test its quality. The resultant Li-ion concentration varied between 1.5 and 15.2 ppm (or mg/L), see Supplementary Fig. S38.

However, the presence of Li ions plays no role in the energy efficiency of water extraction, and our work demonstrates that our methodology is equally applicable to Li-free hydrogels such as HG-M. Our future work will focus on the synthesis and testing of Li-free sorbents with high water uptake to limit the risk of water contamination and to reduce the cost of the technology.

1.10. Supplementary Note 10 – Contributions of mechanical actuation and heating of the device

With the hardware configuration shown in the circuit diagram in Fig. S39 (a), we measured that approximately 300 mW of the supplied 1.5W DC power enters the piezoelectric ultrasound device. Based on our estimated effective coupling coefficient for the PZT device, the actuator efficiency (η_a) — that is, the ratio of electrical energy consumed to the mechanical energy produced — is $\eta_a = k_{eff}^2 = 3.6\%$. In the case of perfect coupling (i.e., $\eta_a = 100\%$), the mechanical loss tangent, $\tan\varphi$, would have been $1/Q = 1/32 = 3.1\%$ (where Q is the quality factor of PZT-5H ceramic), and 3.1% of the input power would be lost as heat[22,23]. Since the actual coupling efficiency is only 3.6%, the actual heat losses are 3.1% of 3.6% plus another portion of the 3.6% associated with work done by the PZT. We assume that the combination of the work done on the hydrogel by the PZT system during its contraction and expansion and the internal mechanical losses of the PZT material itself comprise roughly 25% of the mechanical energy, which is lost as heat, i.e., 25% of 3.6% (i.e., 0.9% of 300 = 2.7 mW). The remaining energy is attributed to mechanical storage, calculated as 2.7% (=3.6% - 0.9%) of 300 mW, which is equal to 8.1 mW.

As piezoelectric devices are essentially capacitors, the bulk of the delivered electrical energy is stored energy, which ultimately returns to the power source. The power delivered to the piezoelectric capacitor is about 96.4% (=100% - 3.6%) of the 300 mW input power, which is 291 mW. The dielectric loss tangent, $\tan\delta_e$, for PZT-5H piezoelectric ceramics is about 2%, and the lost power is dissipated as heat, generating about 5.8mW, i.e., 2% of 291 mW. Hence, the combined mechanical and dielectric power loss to heat is therefore about $5.8\ mW + 2.7\ mW = 8.5\ mW$ when the actuator is driven at its resonant frequency.

In summary, we estimate the energy consumption to be roughly equally divided between the mechanical actuation and heating, with individual contributions measuring 8.1 mW (49%) and 8.5 mW (51%), respectively, while 283.4 mW were returned to the power source (Fig. S39b). Due to the complexity of quantifying the dynamic interaction between the ceramic, the metallic membrane, and the hydrogel during actuation we offer this relatively simplistic analysis to quantify the individual contributions of work, mechanical losses, and dielectric losses. Future work will aim to develop a more comprehensive model to decouple the different effects of heat and vibration on different actuators and sorbents.

1.11 Supplementary note 11 – Solar-thermal energy conversion efficiency calculation

This note discusses the efficiency of the process of solar-thermal energy conversion. Figure S40a illustrates a schematic of a solar absorber modeled as an ideal thermal engine. The energy is delivered to the engine via solar radiation, and the entropy is transferred to the environmental

heat sink via heat conduction. The absorber heats up to a steady-state temperature T_A and emits photons back to the environment in the form of incoherent thermal radiation. A general expression for the efficiency of this engine takes the following form:

$$\eta_{S-T} = \frac{W}{I_S} = \frac{1}{I_S}\left(I_S - \left[I_A(T_A) + T_a\left[S_S(T_S) - S_A(T_A) + S_g\right]\right]\right)$$

Here, I_S and S_S are the solar energy flux and the corresponding entropy flux, respectively. $T_S = 5779\ K$ is the Sun's effective emission temperature. T_A is the temperature of the solar absorber emitting energy flux I_A and the corresponding entropy flux S_A. For the blackbody thermal emission process, $I_A = \sigma T_A^4$ and $S_A = \frac{4}{3}\sigma T_A^3$, where σ is the Boltzmann constant.

The entropy flux of thermal radiation S_A is calculated via integration over photon energy and direction of light propagation, and deviates from the conventional definition of the entropy for thermal processes driven by heat conduction, which would result in the expression $S = \frac{I}{T} = \sigma T^3$. While the Sun is a blackbody, angular and spectral filtering of solar radiation arriving to the Earth surface reduces its entropy dramatically, to $S_S = \frac{4}{3}\frac{\Omega_0 cos\,\theta_0}{\pi}\sigma T_S^3$, where the global averaged cosine of solar zenith angle is $cos\,\theta_0 = 0.25$, and the solar solid angle is $\Omega_0 = 6.77 \cdot 10^{-5}$ sr.

Entropy generated in the process of solar energy absorption in a blackbody absorber and partial re-emission back to the environment in the form of thermal emission can be calculated as follows:

$$S_g = I_S\left(\frac{1}{T_A} - \frac{4}{3}\frac{1}{T_S}\right) + \frac{1}{3}\frac{I_A}{T_A}$$

This combination of energy loss through thermal re-radiation and entropy generation during the photon absorption-emission process significantly restricts the maximum efficiency of the solar-thermal energy conversion. For comparison, I_S can reach 1,000 W/m² on a clear day at solar noon and is lower in the presence of clouds or during early/late hours of the day. In turn, the energy flux I_A emitted by a blackbody absorber at 60°C (which is a typical temperature used for sorbent regeneration) is approximately 687.6 W/m². As a result, the solar-thermal energy conversion efficiency reaches a limit of only ~15% for a blackbody absorber illuminated by sunlight without concentrating optics (i.e., under one sun illumination)[24,25], see Fig. S40b.

Solar concentration using external lenses or reflectors can increase the absorber temperature by focusing sunlight and increasing the solar energy flux per surface area (Fig. S40c). This results in the increased efficiency of soler-thermal energy conversion (Fig. S40b), but requires installation of additional components, such as solar concentrators and trackers, increasing the system cost and footprint.

To suppress re-emission losses, solar absorbers with a stepwise emittance spectrum can be engineered[25–29], which exhibit high absorptance across most of the solar spectrum, and zero emittance at lower frequencies overlapping with the thermal emission spectra. As illustrated in Figs. S40b,c, an absorber with 90% solar absorptance and 10% infrared emittance can increase the

maximum possible efficiency of the solar energy conversion. Note that due to the presence of atmospheric absorption bands in the solar spectrum, the equilibrium temperature does not vary smoothly with the solar concentration, as evidenced by the kinks in Fig. S40c[30]. However, water has very high infrared emittance[22], making this strategy inapplicable to engineering AWH sorbents.

For comparison, as illustrated in Fig. S40b, the PV conversion efficiency of solar energy to electricity reaches about 20-25% for a single-junction commercial PV cell under 1-sun unconcentrated sunlight illumination[31–35]. It can be further increased if multiple-junction PV cells are used under concentrated sunlight, and the energy can be either used immediately or stored for use during nighttime.

2. Supplementary Tables

2.1. Supplementary Table 1. Geometry of the metal membranes and piezoelectric rings.

Device	Frequency	Piezoelectric ring			Membrane mesh			
	(KHz)	Thickness (mm)	Outer diameter (mm)	Inner diameter (mm)	Thickness (mm)	Membrane & mesh diameters (mm)	Nozzle no	Nozzle size (µm)
PZ-A	107-113	0.6	16	7.8	0.05	16, 5	1000	10
PZ-B	107-113	0.6	16	7.8	0.05	16, 5	1000	70
PZ-C	107-113	0.6	16	7.8	0.05	16, 5	1000	100
PZ-D	165-170	0.6	11.6	5	0.05	13.8, 5	1000	10

2.2. Supplementary Table 2. Mass of the actuator and its major components.

Device	PZT ring (g)	Membrane (g)	Entire actuator (g)
PZ-A	0.715±0.013	0.079±0.012	1.172 ±0.019
PZ-B	0.709±0.011	0.078±0.008	1.169 ±0.016
PZ-C	0.713±0.011	0.077±0.005	1.169 ±0.011
PZ-D	0.381±0.012	0.059±0.004	1.088±0.012

2.3. Supplementary Table 3. Vibrational mode assignments in the FTIR spectra of HG-A hydrogels.

Peak	Wavenumber	Description
1	3584 cm^{-1}	Asymmetric O–H stretching modes of weakly or non-hydrogen-bonded water molecules (HBs of the water molecules are partially or entirely broken)
2	3504 cm^{-1}	Symmetric O–H stretching modes of weakly or non-hydrogen-bonded water molecules (HBs of the water molecules are partially or entirely broken)
3	3427 cm^{-1}	Out-of-phase O–H stretching modes of water molecules with four HBs
4	3353 cm^{-1}	Asymmetric stretching modes of NH_2
5	3279 cm^{-1}	In-phase O–H stretching modes of water molecules with four HBs
6	3206 cm^{-1}	Symmetric stretching modes of NH_2
7	3129 cm^{-1}	An overtone of the O–H stretching mode at 3261 cm^{-1}
8	3106 cm^{-1}	C–H stretching modes of the polymer chains (three modes, i.e., one C–H stretching mode of the CH groups and symmetric and asymmetric stretching modes of the CH_2 groups)

2.4. Supplementary Table 4. A summary of variables derived from literature to derive specific energy consumption and the efficiency of the devices for water release process in comparison to our devices.

Reference	Water production (kg/day)	Energy input (kWh/day)	Specific energy consumption (kWh/kg)	Efficiency η (%)
LaPotin et al. [36]	0.06	0.421	7.02	9.5
Hanikel et al. [37]	0.41	10.79	26.32	2.4
Xu et al. [38]	0.023	0.36	15.65	4.0
Shan et al. [39]	0.311	3.475	11.17	5.6
Almassad et al. [40]	0.72	12.456	17.3	3.6
This work for HG-M [a]	0.00013*	0.000175*	1.35	47
This work for HG-A [b]	0.00013*	0.000188*	1.44	43
This work for HG-A [c]	0.00014*	0.000188*	1.44	43
This work for HG-A [d]	0.00004*	0.000013*	0.31	200
This work for HG-A [e]	0.00007*	0.000038*	0.54	117
This work for HG-A [f]	0.00094	0.000138	0.15	428.6

* Per cycle

[a] After 10-min actuation cycle using a single device

[b] After 25-min actuation cycle using a single device

[c] After 10-min actuation cycles using an array made of three devices

[d] After 2-min actuation cycle using a single device

[e] After 2-min actuation cycle using an array made of three devices

[f] Measured over 11-hr period utilizing a large specimen and eleven 2-min actuation cycles (i.e., 22 min over 11hr)

2.5. Supplementary Table 5. A summary of water harvesting cycles of larger HG-A (>16 mm diameter) sorbent.

	HG-A Specimen 1	HG-A Specimen 2	Average values
Collection per device per hour [g]	0.12	0.13	0.125
Collection per device per 40 minutes [g]	0.08	0.087	0.0835
Collection per device for 34 cycles [g]	2.77	2.96	2.865
Extraction per device per 2 min [g]	0.074	0.085	0.0795
Extraction per device for 34 cycles [g]	2.52	2.91	2.715
Collection per m^2 per day for 34 cycles [kg]	3.07	3.26	3.165
Extraction per m^2 per day for 34 cycles [kg]	2.77	3.19	2.98
Specific energy consumption [kWh/kg]	0.171	0.148	0.160

2.6. Supplementary Table 6. A summary of water harvesting cycles of smaller HG-A (≤16 mm diameter) sorbent.

	HG-A Specimen 1	HG-A Specimen 2	Average values
Collection per device per hour [g]	0.012	0.013	0.0127
Collection per device per 118 minutes [g]	0.024	0.026	0.025
Extraction per device per 2 minutes [g]	0.029	0.033	0.031
Collection per device per day [g]	0.289	0.31	0.3
Collection per m^2 per day [kg]	1.447	1.549	1.523
Specific energy consumption [kWh/kg]	0.426	0.396	0.411

2.7. Supplementary Table 7. Comparison of water productivity among different studies.

Sl	RH%	AWH per sorbent (L kg^{-1} day^{-1})	AWH per area (L m^{-2} day^{-1})	Reference	Water harvesting configuration
A	80	0.09	2.8	[41]	Single rectangular liquid sorbent bed of [EMIM][Ac]
B	70-90	0.22	2.25	[42]	Rolled-up 4-pcs of ACF-$CaCl_2$ sorbent bed
C	<20	0.07	0.35	[43]	Single MOF-801 sorbent bed
D	57-68	0.12	0.7	[36]	Vertically stacked 2-pcs of AQSOA Z01 zeolite bed
E	10-40	0.25	0.34	[44]	Single rectangular MOF-801 sorbent bed
F	30	0.45	0.4	[45]	Single circular pot of LiCl@MIL-101(Cr)
G	10	0.7	0.43	[37]	A modular MOF-303 exchanger cartridge
H	60	0.83	1.02	[46]	A rotational cylinder loaded with LiCl capsule sorbent
I	40-70	1.05	0.7	[47]	Batchwise continuous production using a sorbent bed made of LiCl@rGO–SA
J	50	0.47	3.7	[48]	Vertically organized 5 sorbent beds made of LiCl@rGO–SA working in batches
K	57	4.05	8.9	[49]	Vertically rotatable sorbent bed made of salt-based HIPG powered by wind at >1 m/s
1R	75	0.73	3.25	This work	One 1-m^2-area row of devices
2R	75	0.73	6.5	This work	Two 1-m^2-area rows of devices
3R	75	0.73	9.75	This work	Three 1-m^2-area rows of devices
4R	75	0.73	13	This work	Four 1-m^2-area rows of devices
5R	75	0.73	16.25	This work	Five 1-m^2-area rows of devices

2.8. Supplementary Table 8. Parameters used in estimating the cost of water production.

Component	Amount used	Price	Ref.
Lithium chloride *	0.8 kg	0.1-1 $/kg	[50]
Acrylamide	0.2 kg	1.6 $/kg	[51]
Ammonium persulfate	0.68 g	0.61 $/kg	[52]
N,N'-methylenebisacrylamide	2.4 g	1 $/kg	[53]
N,N,N',N'-tetramethylethylendiamin	0.57 mL or 0.44 g [54]	10 $/kg	[55]
Ultrasonic system *	1 unit	1-2 $/unit	[56]
Electricity cost **	0.00025 kWh	0.0002 $/10min	[57]

* The price fluctuated during the study duration

** Estimated for a single unit

3. Supplementary Figures

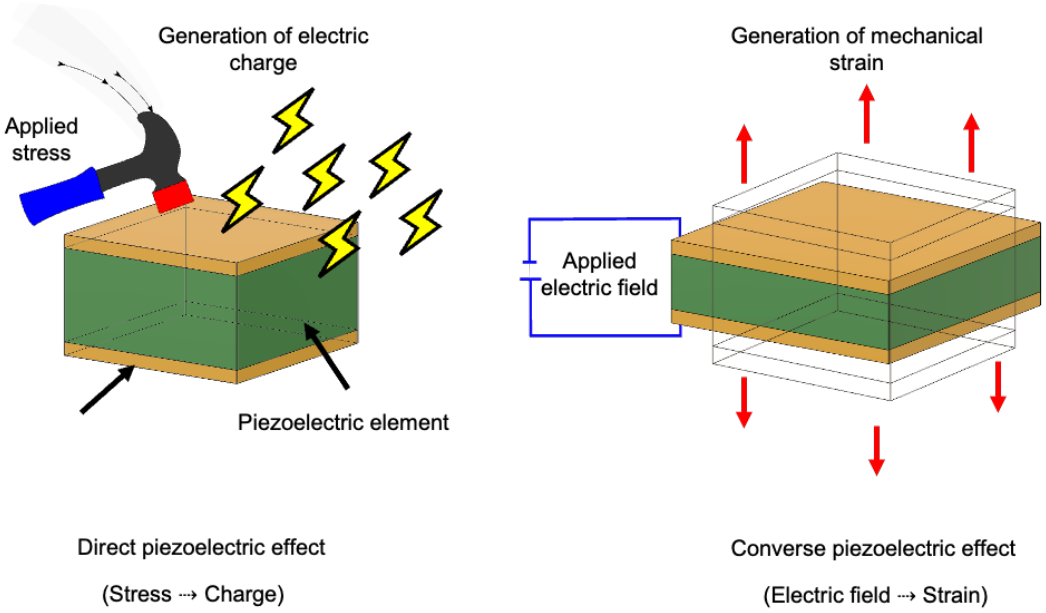

Supplementary Figure S1. Direct (left-sensor) and converse (right-actuator) piezoelectric effects. We utilized the converse piezoelectric effect to actuate the water-harvesting hydrogel placed on top of a piezoelectric transducer and to expel water out of it. In addition, we made use of the direct piezoelectric effect to achieve *in-situ* monitoring of the changes in the weight of the hydrogel throughout the process of atmospheric water harvesting. Subsequently, we employed the acquired sensing information to train our deep neural network designed for hydrogel classification.

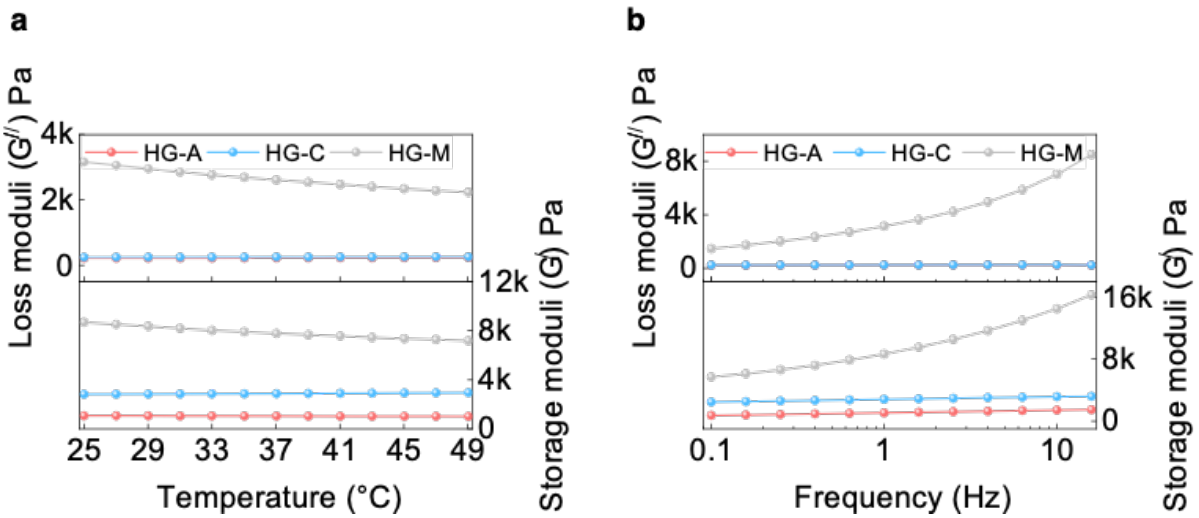

Supplementary Figure S2. Rheological performance of the PAM-LiCl (HG-A and HG-C) and commercial hydrogels (HG-M). a-b. Modulus changes of the hydrogel specimens as a function of temperature (a) and frequency (b).

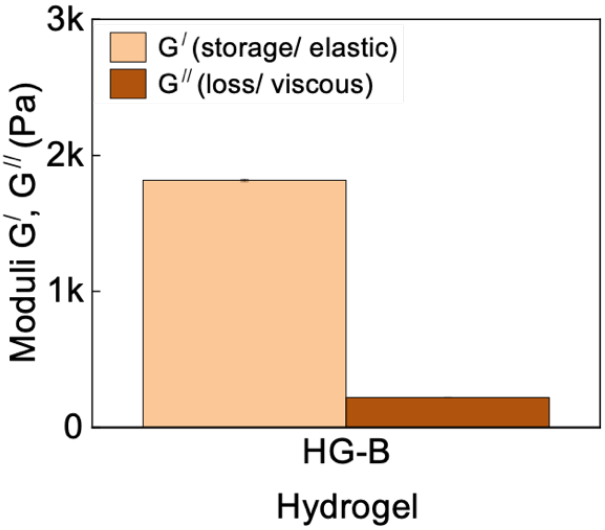

Supplementary Figure S3. Storage (light brown) and loss (dark brown) moduli of the HG-B hydrogel specimen.

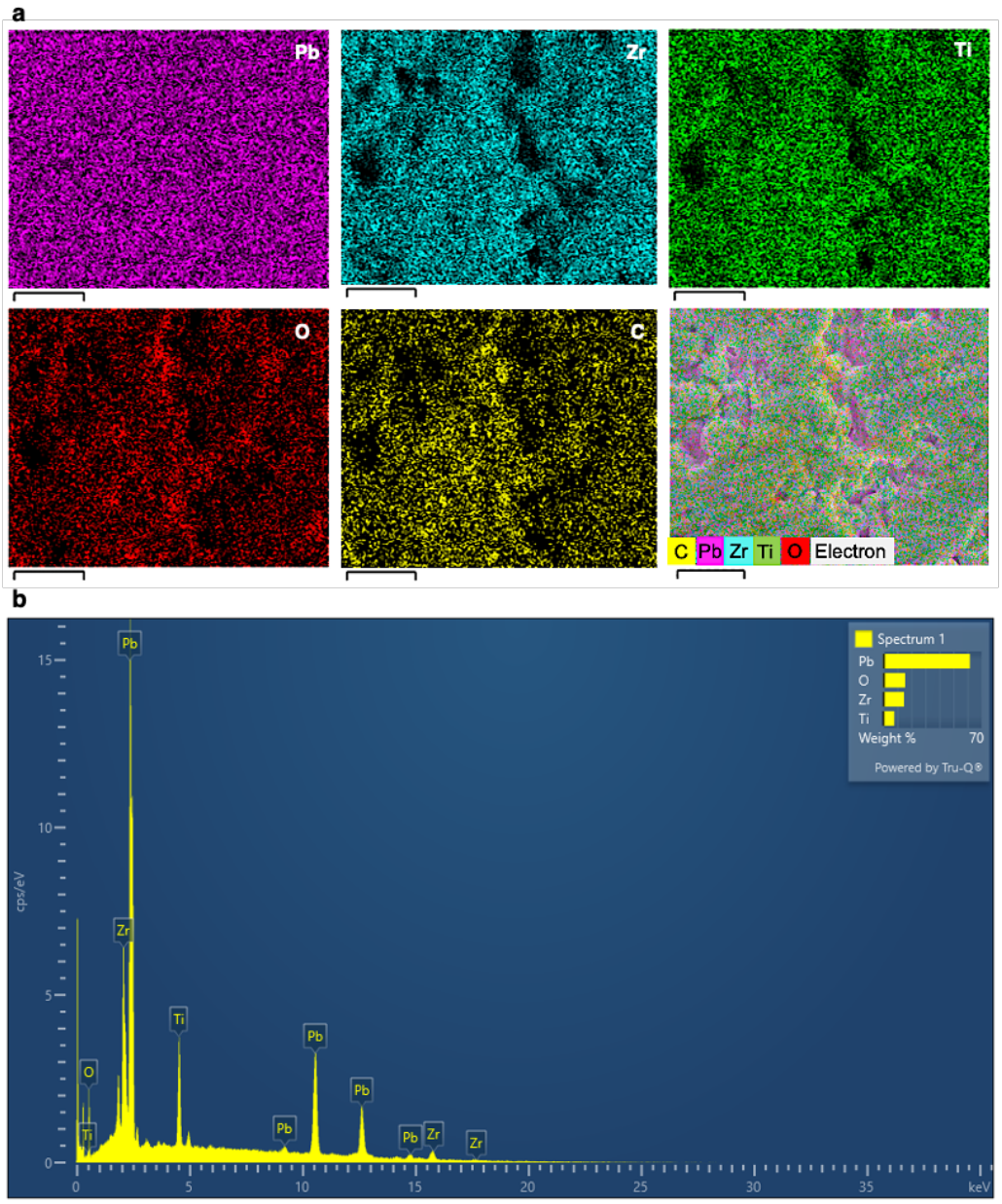

Supplementary Figure S4. Energy dispersive X-ray spectroscopy (EDS) of PZT polycrystal used in this study. **a**. Composition mapping of different elements (Pb, Zr, Ti, O, C) and their layered EDS image. **b**. The corresponding EDS spectra. Scale bars: 10 μm.

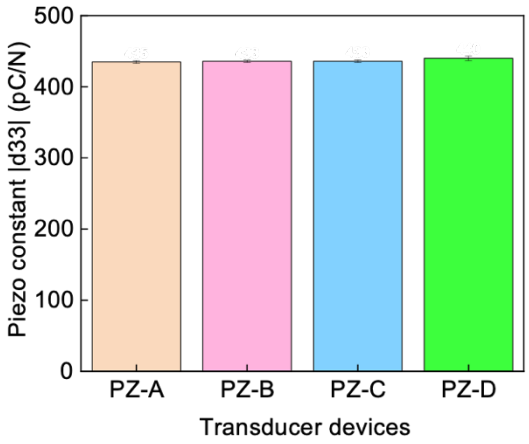

Supplementary Figure S5. Measured piezoelectric charge coefficients (pC/N) of the bare ceramic materials employed in fabricating the four transducers (PZs- A, B, C, and D). This comparative analysis demonstrates that despite minor variances in the operating frequency and geometry, the piezoelectric coefficients are comparable among all the transducers.

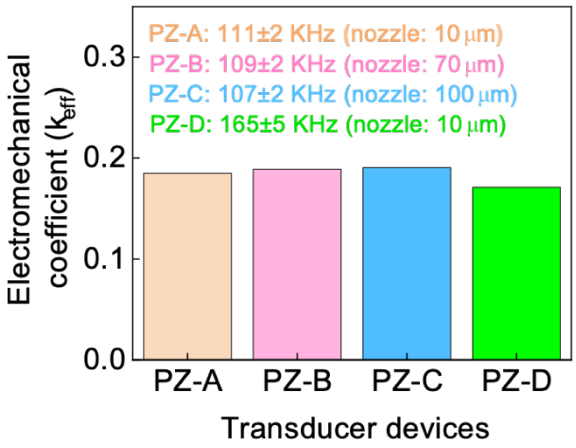

Supplementary Figure S6. Effective electromechanical coupling co-efficient of the four actuator devices (PZs- A, B, C, and D). This comparative analysis demonstrates that regardless of the nozzle size, the coupling coefficients are comparable for all the low-frequency transducers or actuators but differ from those of the high-frequency actuators.

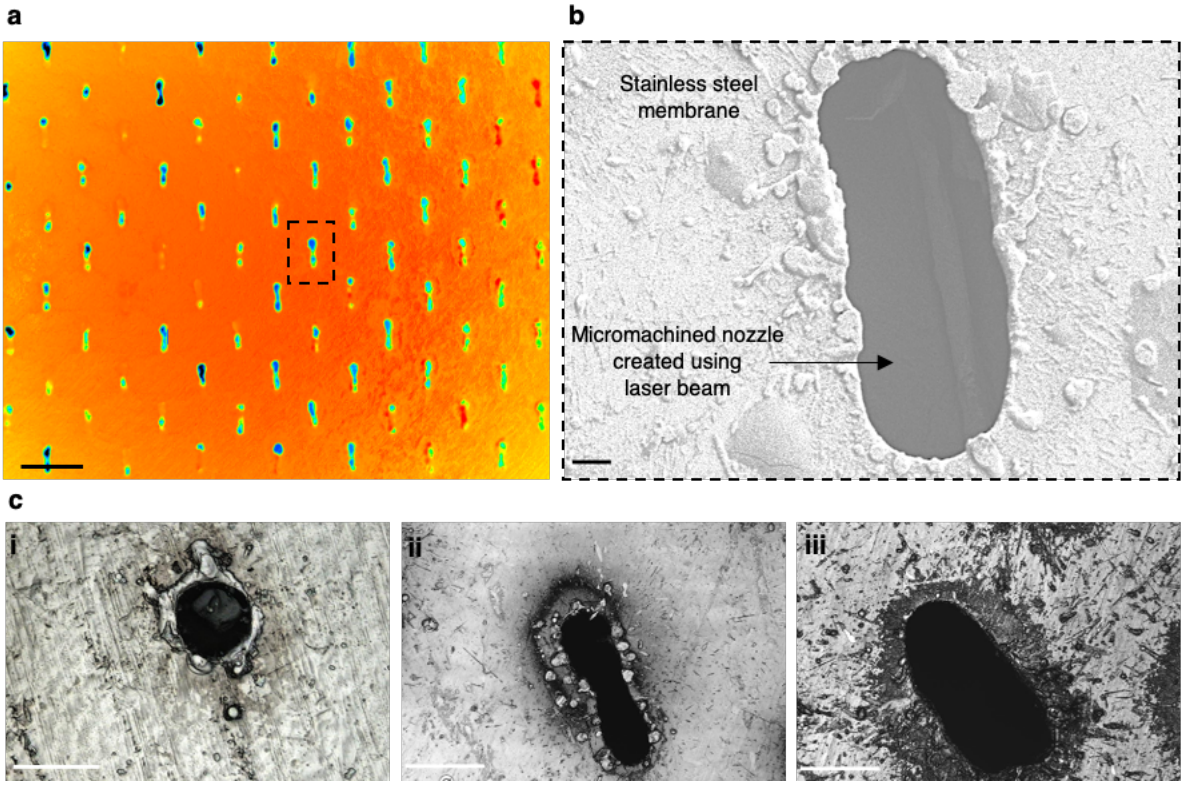

Supplementary Figure S7. Microscopic imaging of porous membranes. **a-b**. A heat map of a porous membrane surface (a) and a SEM image of a single nozzle of the membrane (b). **c**. Confocal laser scanning microscopy (CLSM) images of the three different nozzles used in three different membranes. Scale bars: 200 µm (a); 10 µm (b); 10 µm (c i); 30 µm (c ii); 50 µm (c iii).

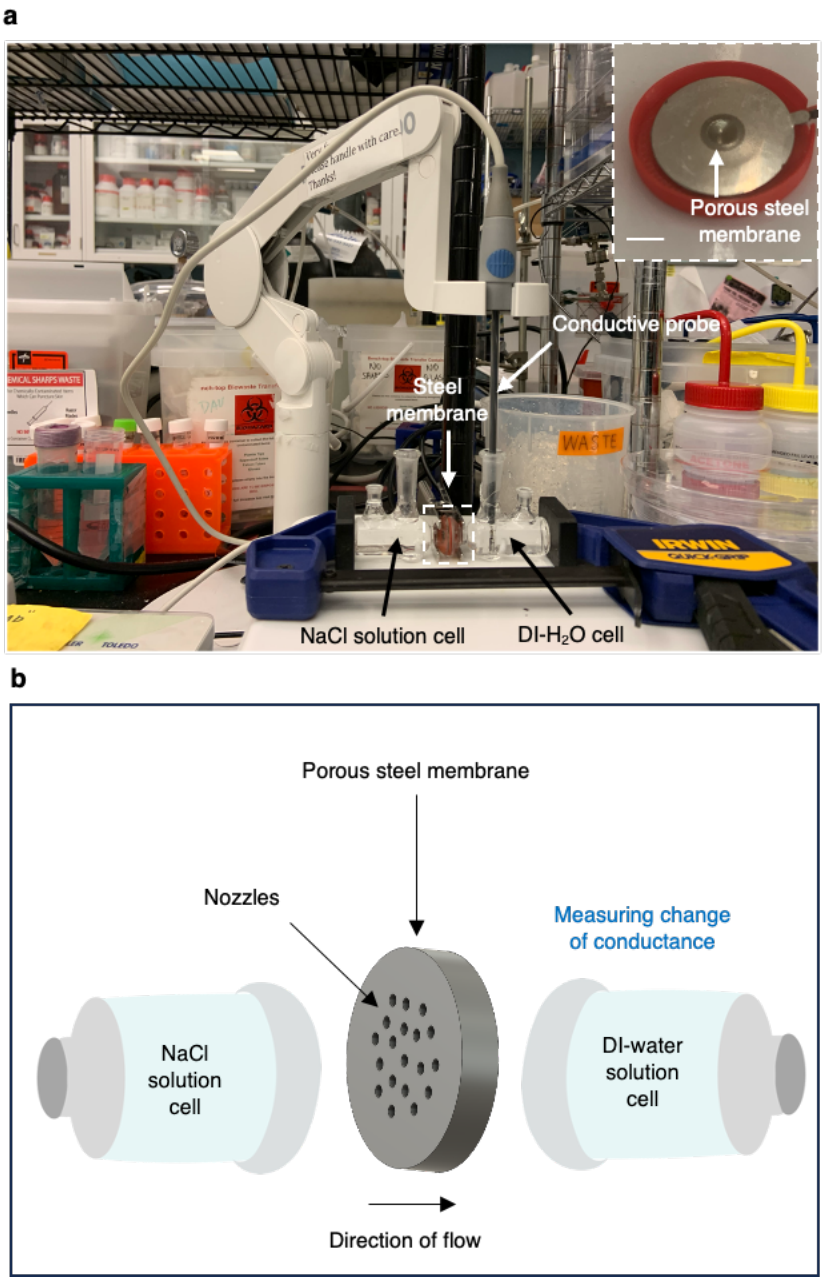

Supplementary Figure S8. Ion-solution permeability test. a. A photograph of a set-up for evaluating water transmission performance through porous membranes with different nozzle sizes. Inset shows an optical image of a bare porous stainless-steel membrane used in this study. **b**. Representative schematic illustrating the flow of ions from left cell to right cell causing change of conductance. Scale bars: 4 mm (a-inset)

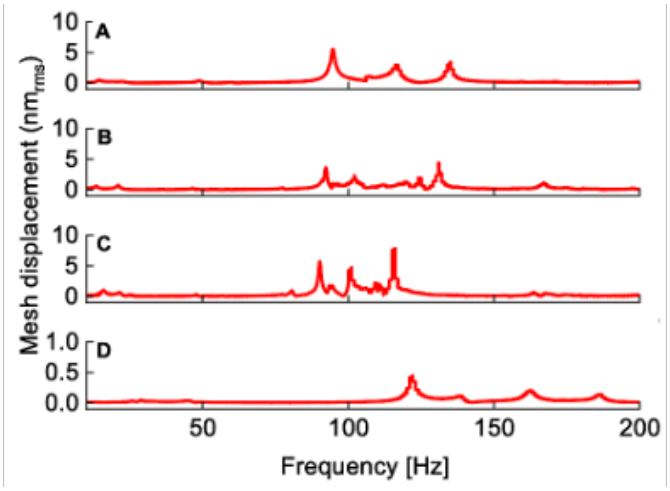

Supplementary Figure S9. Out-of-plane local (single point) modal analysis at the center of the membrane mesh (M) for PZs- A, B, C, and D transducers. The frequencies are obtained by performing a Fast Fourier transform (FFT) on the time-domain data.

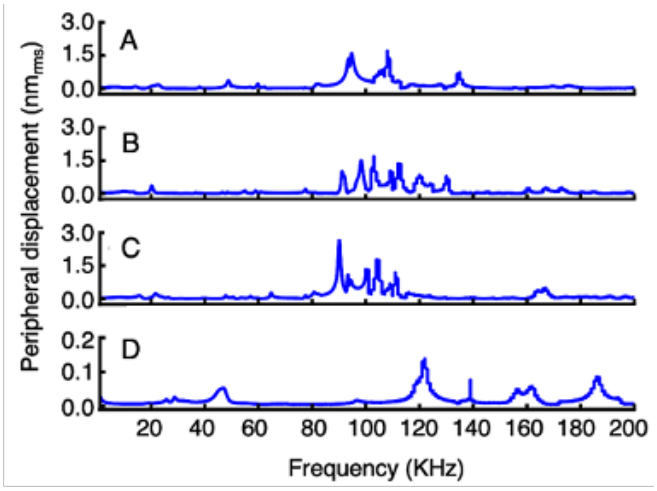

Supplementary Figure S10. Out-of-plane local (single point) modal analysis at the periphery (P) of the membrane for PZs- A, B, C, and D transducers. The resultant frequencies are obtained by performing a Fast Fourier transform (FFT) on the time-domain data.

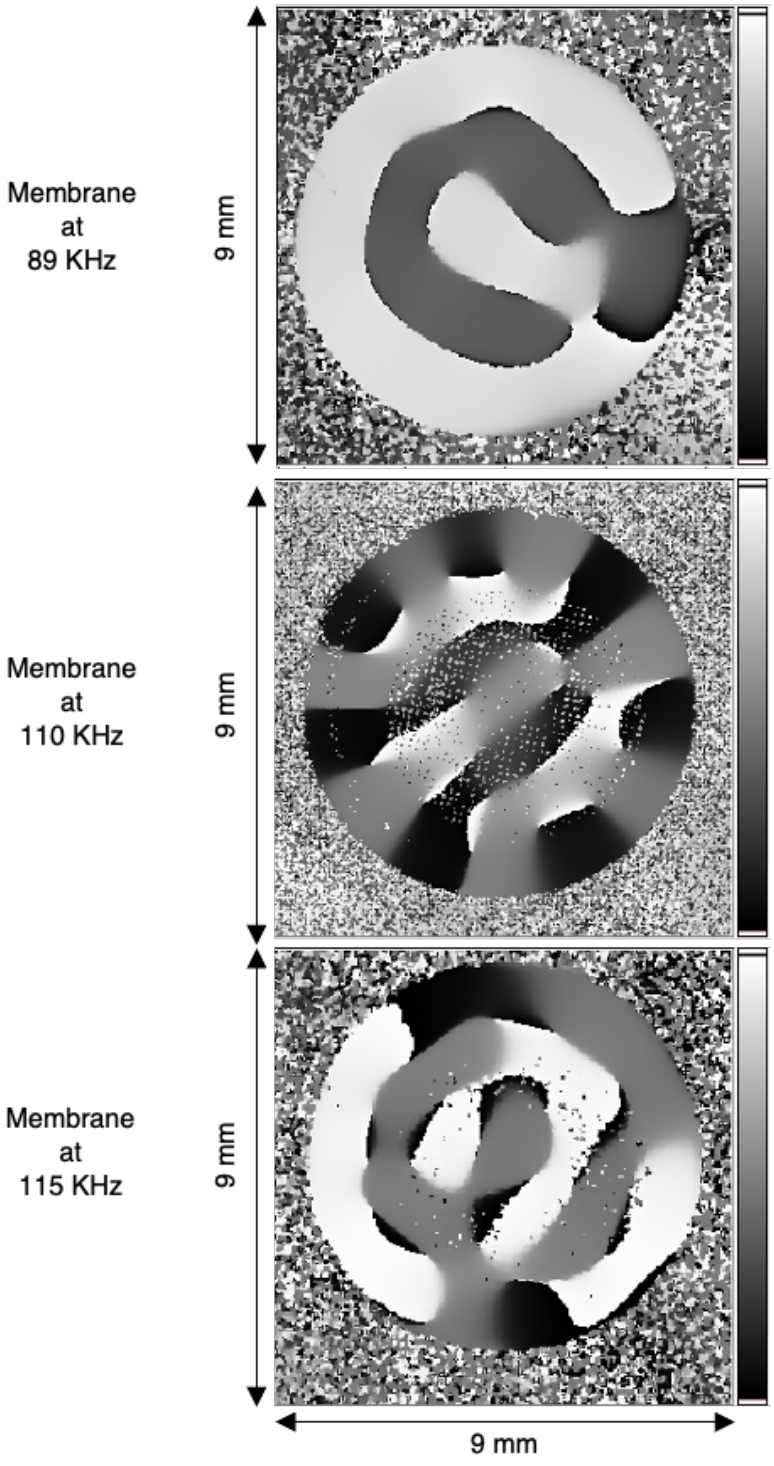

Supplementary Figure S11. Out-of-plane phase change during the global modal analysis of the membrane. The modal analysis was conducted at three different frequencies: 89, 110, and 115 kHz (from top to bottom). The corresponding representative animations of the out-of-plane deflection patterns of the vibrating membrane are included as Supplementary Movie 4.

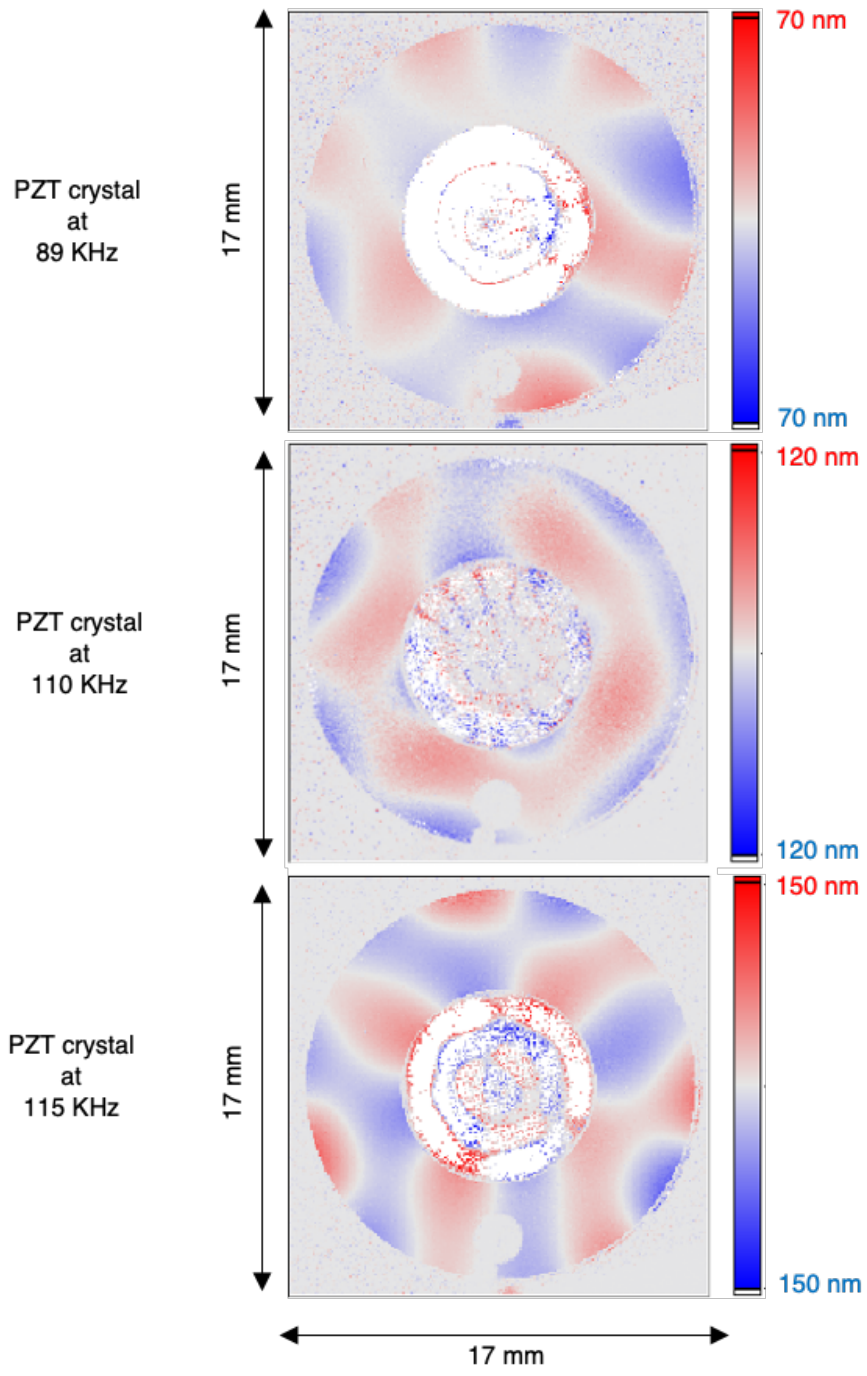

Supplementary Figure S12. Out-of-plane global modal analysis of the entire ring PZT crystal (16 mm in diameter). The modal analysis was conducted at three different frequencies: 89, 110, and 115 kHz (from top to bottom). The data reveal that the out-of-plane longitudinal (thickness mode) deflection of the PZT is extremely low compared to longitudinal deflection of the steel membrane. The corresponding representative animations of the out-of-plane deflection patterns of the vibrating PZT are included as Supplementary Movie 5.

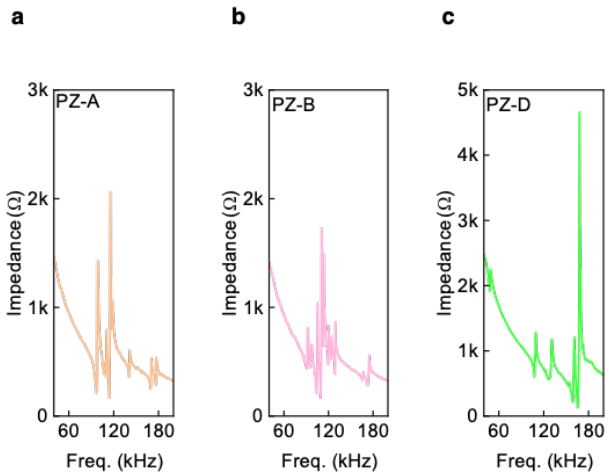

Supplementary Figure S13. Frequency-impedance spectra of PZ-A, B, and D (a-c) actuators.

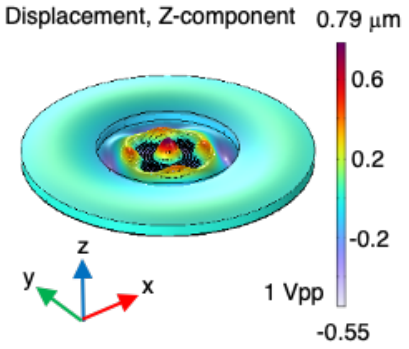

Supplementary Figure S14. Simulated deflection amplitude of a PZ-C actuator under 1 V_{pp} electric stimulation. We used the COMSOL Multiphysics® software to perform the modeling[58].

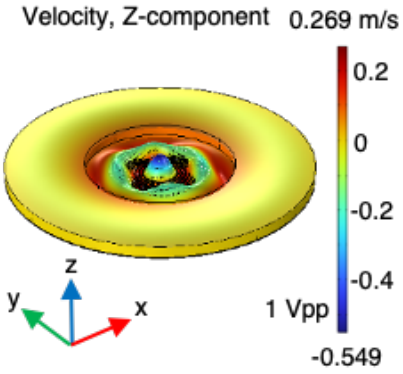

Supplementary Figure S15. Simulated (COMSOL Multiphysics®) velocity of a PZ-C actuator under 1 V_{pp} electric stimulation.

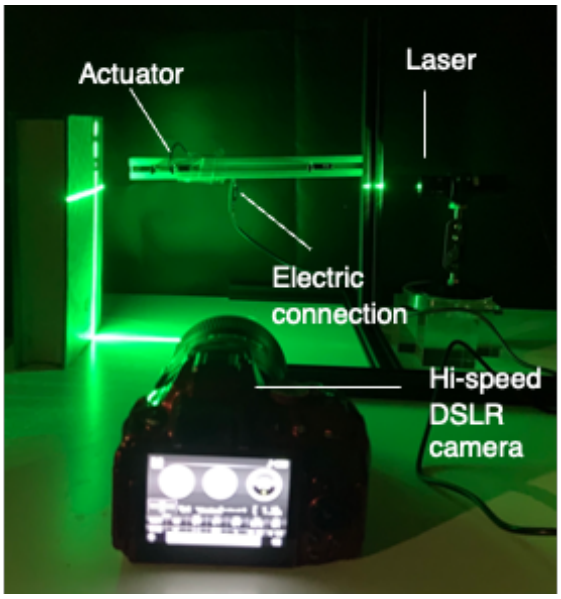

Supplementary Figure S16. High-speed photography setup. The setup allows capturing and recording water droplet ejection through the nozzles of piezoelectric actuator, which cannot be seen by the naked eye.

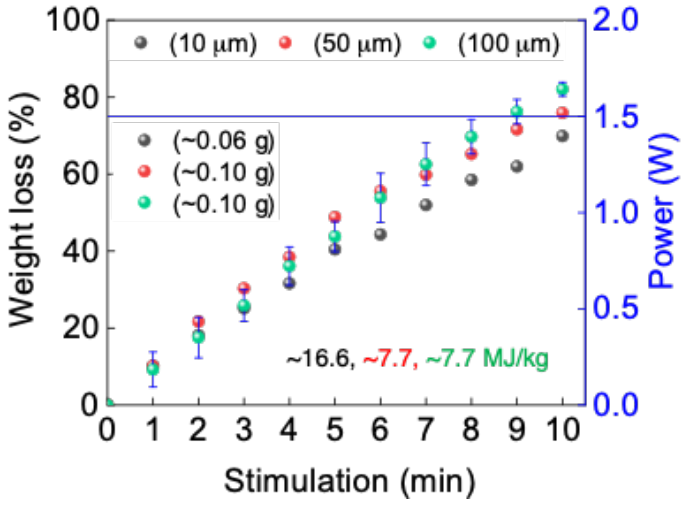

Supplementary Figure S17. Water extraction using commercial hydrogels (HG-M) with actuators (PZs- A, B, and C) under a constant 1.5 W power. The plot shows the desorption capabilities as a function of the nozzle size of the meshed membrane (data shown for 10, 50, and 100 μm nozzles).

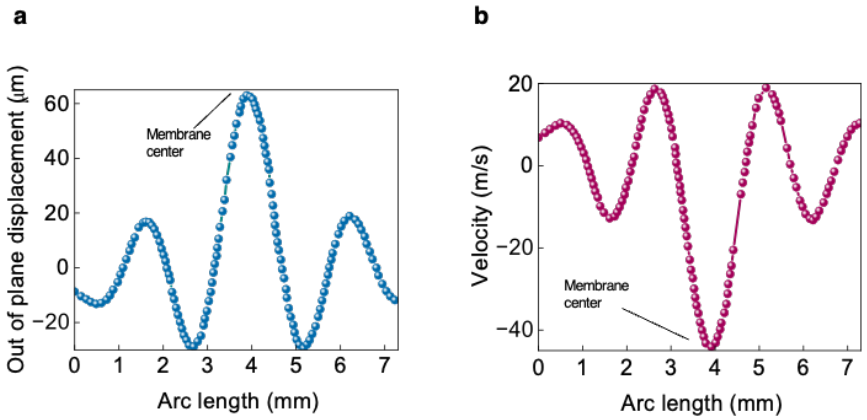

Supplementary Figure S18. Simulating (COMSOL Multiphysics®) the real-life dynamic behavior of the piezoelectric actuator operating at ~114 V_{pp} at operating frequency of ~110 KHz. a-b. The predicted mechanical deflection (a) and the corresponding velocity of the actuator (b) obtained from a 3D FEM model.

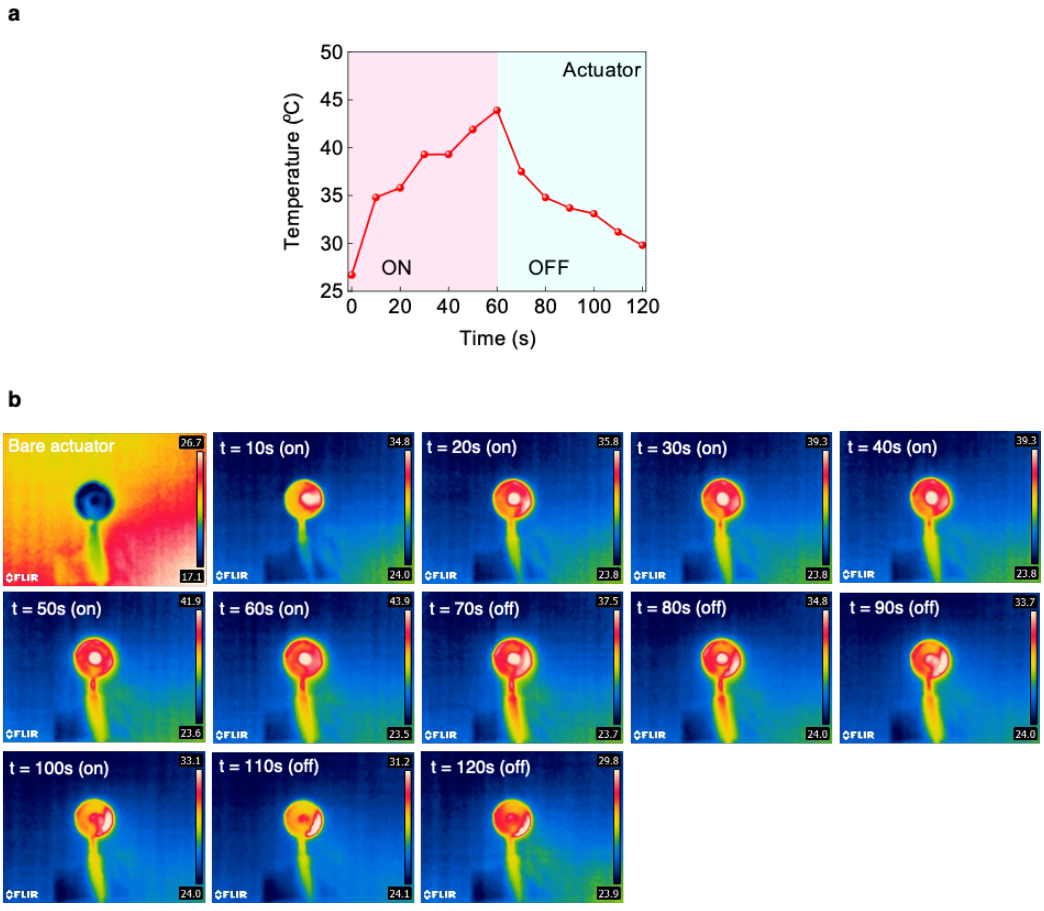

Supplementary Figure S19. Joule heating performance of the actuator. **a**. Time-temperature profile curve of the actuator demonstrating fast heating and cooling capability. **b**. IR thermographs acquired during the heating and cooling process. Colormap is in units of Celsius (°C).

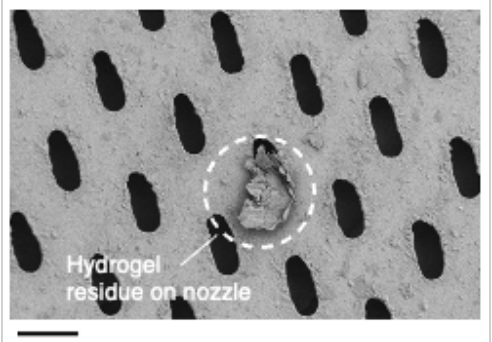

Supplementary Figure S20. Scanning electron micrograph (SEM) of the membrane nozzle after a water extraction cycle from a hydrogel specimen. The image shows negligible amount of hydrogel residue on the nozzle. Scale bar: 16 mm.

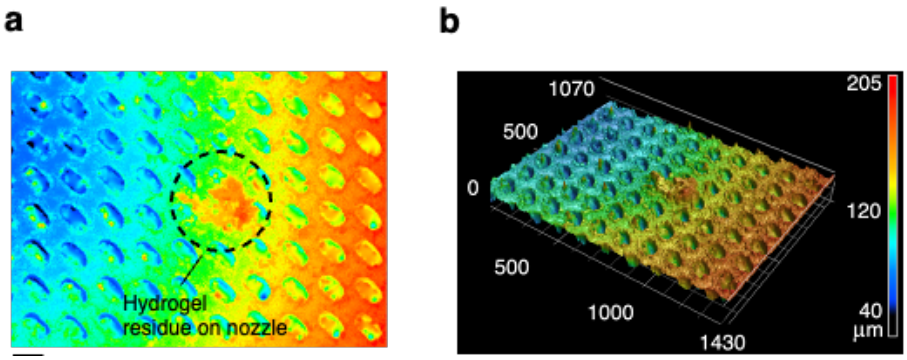

Supplementary Figure S21. Laser scanning confocal microscopy for non-contact surface profiling of a membrane nozzle following water extraction from a hydrogel specimen. a-b. The spatial maps of surface topography (a) and surface roughness (b). Scale bar: 100 µm (a-b).

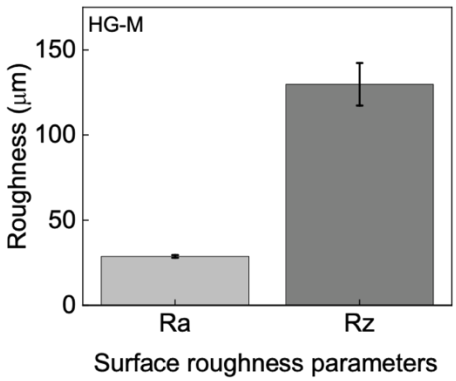

Supplementary Figure S22. Measured roughness of the membrane nozzle after the water extraction cycle from a hydrogel specimen. Following the assessment of multi-line roughness measurements, the arithmetic mean roughness (Ra) (i.e., average variation in profile height from the centerline) and the maximum roughness (Rz) (i.e., vertical distance between the highest and lowest points of the profile) were determined to be 28.7±0.8 and 129.8±12.5 µm, respectively.

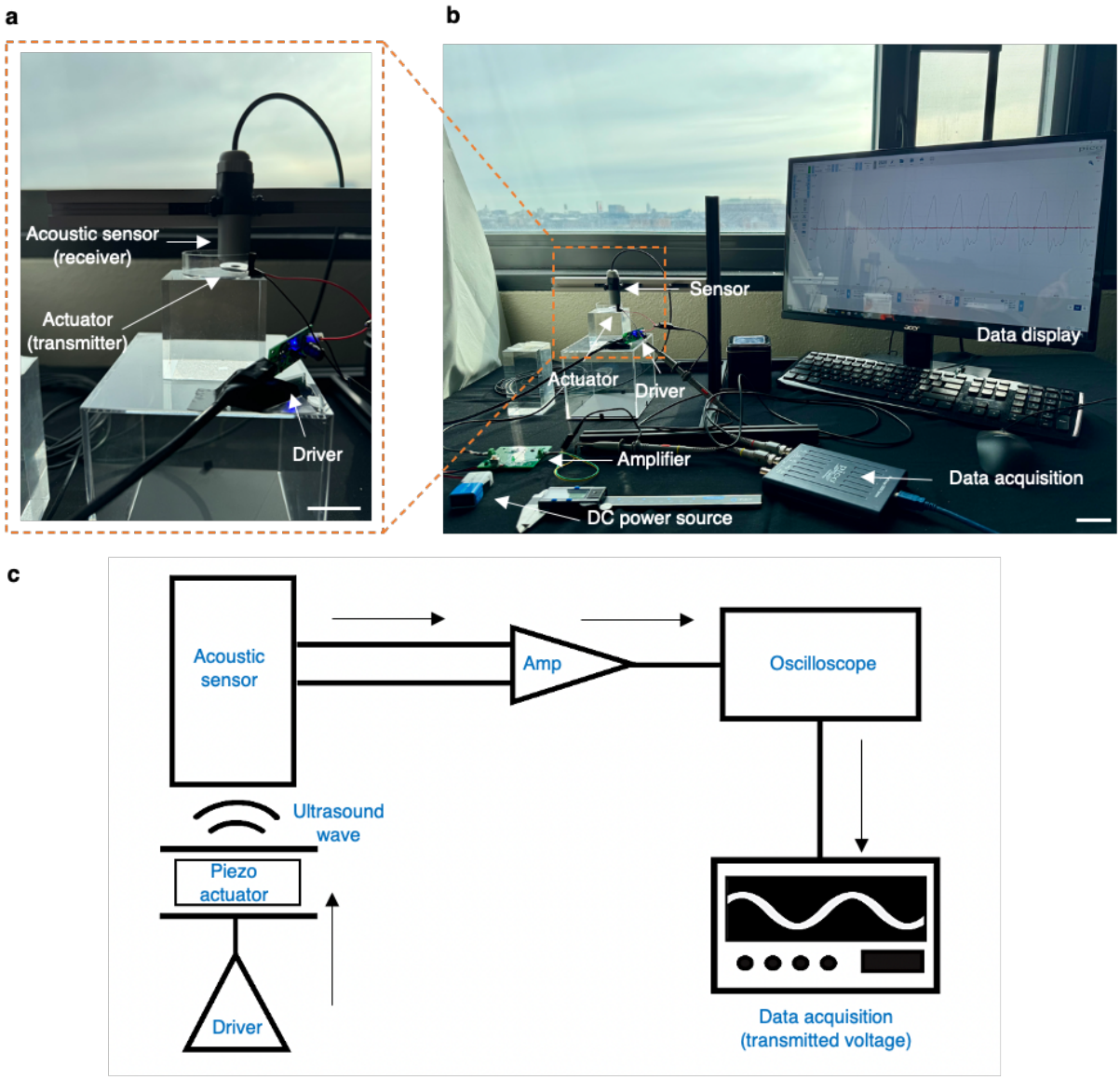

Supplementary Figure S23. Acoustic radiation measurement test. a. Photograph of an acoustic sensor used to measure the acoustic radiation from the piezoelectric transmitter. **b**. A photograph of the test setup showing hydrogel specimens sandwiched between the sensor and the transmitter to evaluate the impact of the hydrogel thickness and rigidity on the acoustic signal transmittance. The transmitted and received waveforms are processed for data analysis. **c**. A representative schematic diagram of the test process and the data acquisition setup. Scale bars: 16 mm (a); 52 mm (b). A representative real-time experimental demonstration of the sensor operation is included as Supplementary Movie 6.

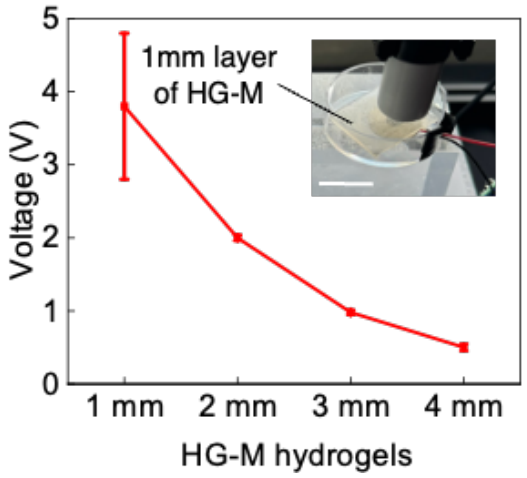

Supplementary Figure S24. The effect of hydrogel thickness on the transmitted voltage from the piezoelectric ultrasonic actuator. The signal is received by the acoustic hydrophone sensor (shown in the inset). Scale bar: 16 mm.

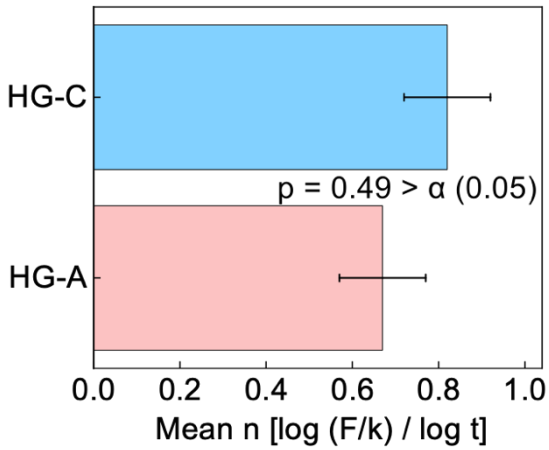

Supplementary Figure S25. An analysis of variance (ANOVA) study to compare the release constants (n) of HG-A and HG-C hydrogel specimens estimated using the Korsmeyer-Peppas (K-P) kinetic model.

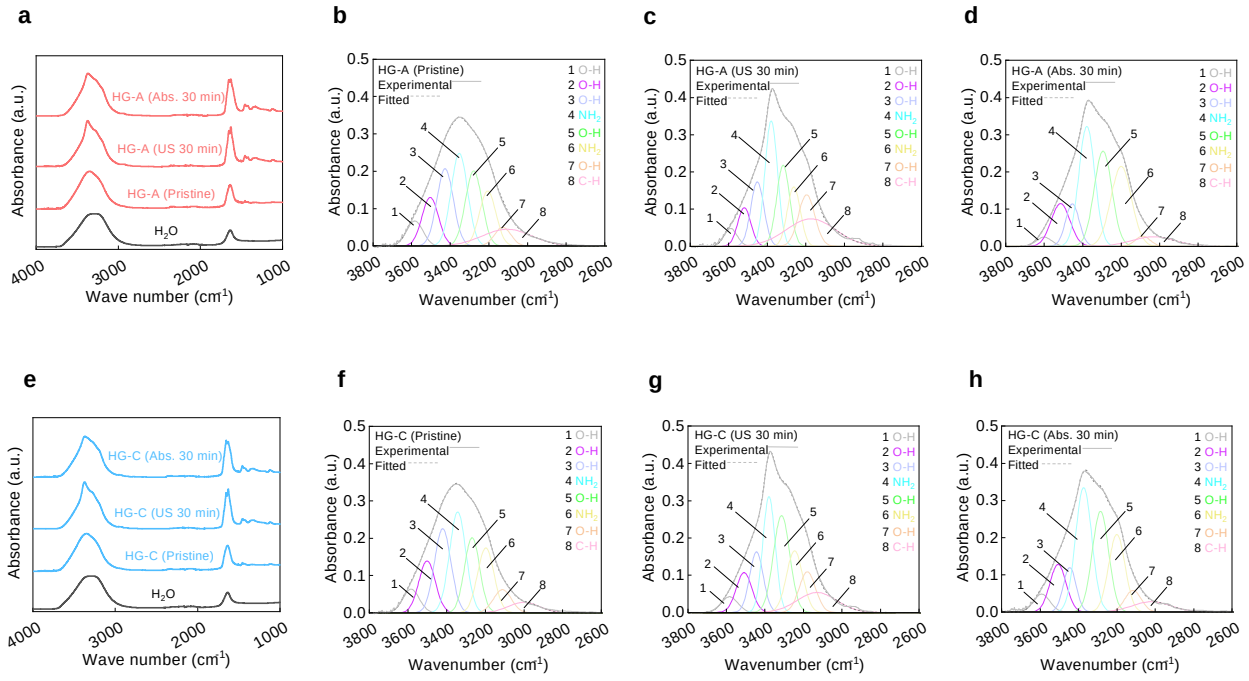

Supplementary Figure S26. a, e. FTIR spectra of liquid DI water, pristine HG-A and HG-C hydrogels, HG-A and HG-C subjected to 30 min of ultrasound exposure, and post-atmospheric water harvesting for 30 min following ultrasound exposure. **b-d, f-h**. Deconvoluted FTIR spectra of HG-A (b-d) and HG-C (f-g) gels during different stages of the sorption-extraction process.

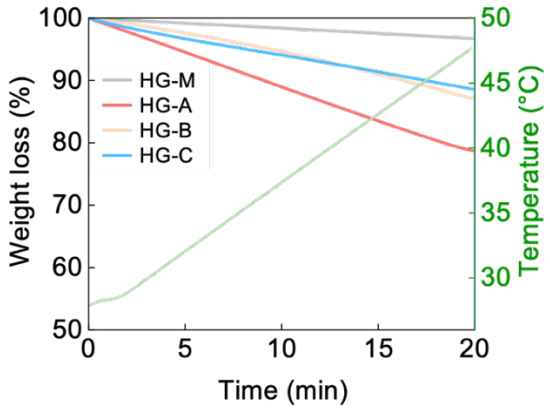

Supplementary Figure S27. Thermogravimetric analysis of the hydrogel specimens with a temperature ramp rate of 1 °C/min. The analysis demonstrates that the high-modulus specimens (HGs-B, C, and M) release less moisture than the low-modulus HG-A specimens.

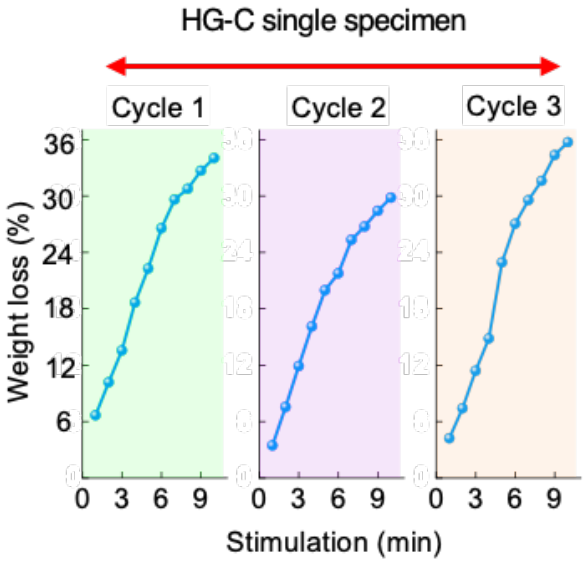

Supplementary Figure S28. Cyclic stability test of a HG-C specimen. The test demonstrates the desorption behavior of the same specimen over three extraction cycles using a common actuator.

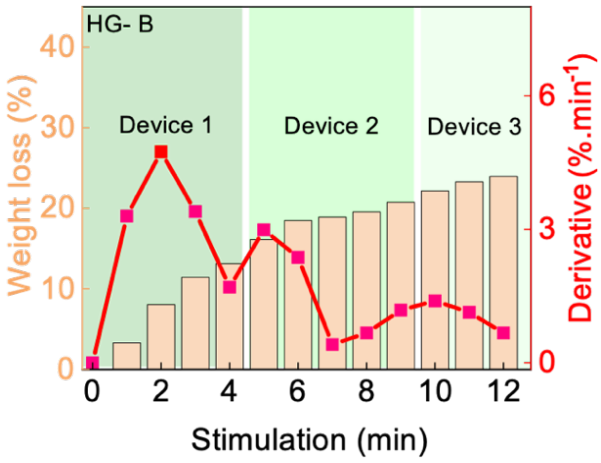

Supplementary Figure S29. Water extraction performance from the HG-B specimen. An erratic water extraction behavior was observed during the actuation process.

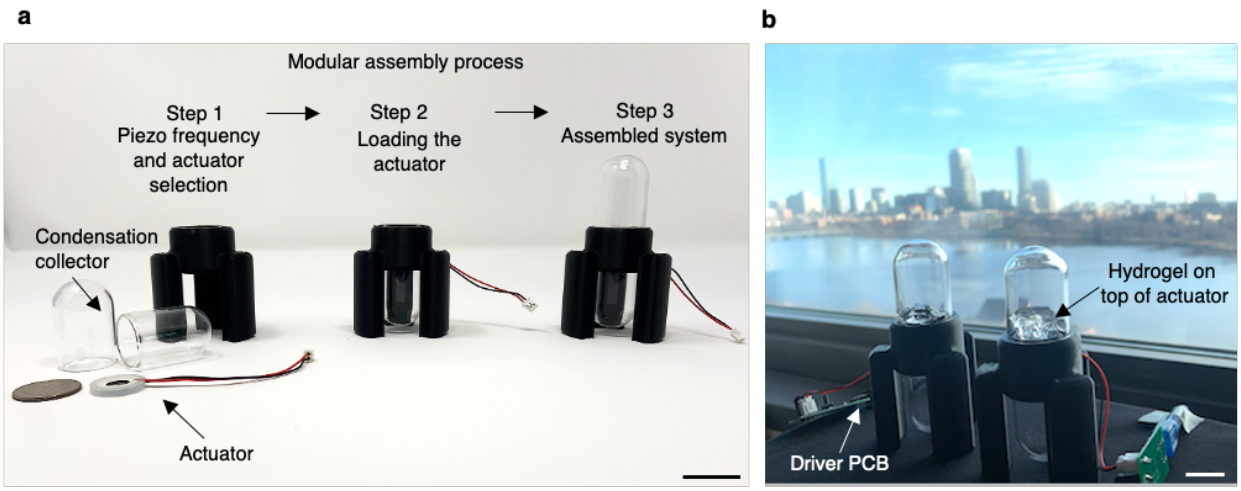

Supplementary Figure S30. A photograph of the ultrasonic actuator system and its assembly process. **a**. The assembly process of the entire system housing a piezoelectric actuator. **b**. A real-life indoor demonstration of the water extraction system using atmospheric water harvesting hydrogels. Scale bars: 16 cm (a-b). A representative animation and real-time demonstration of the water extraction system are included as Supplementary Movie 7.

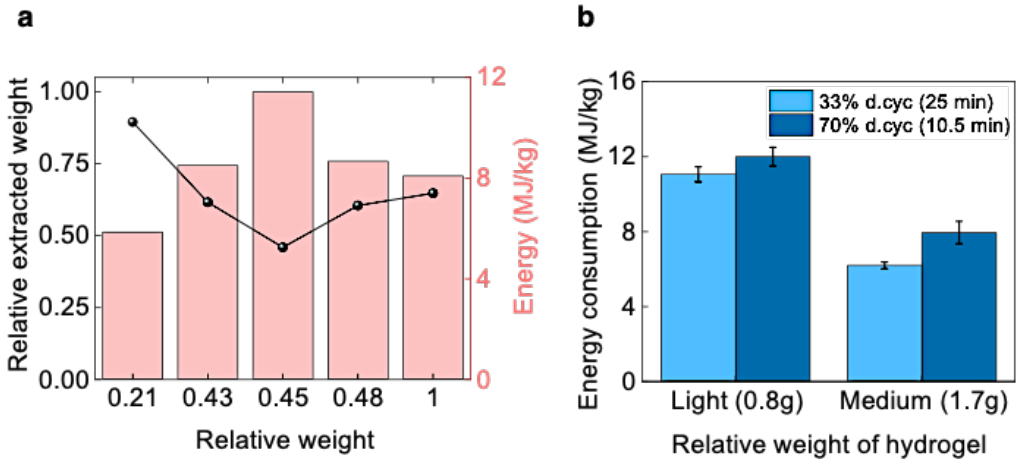

Supplementary Figure S31. a-b. Minimization of the energy consumption by optimizing the sample mass (**a:** HG-A specimen; **b:** HG-C specimen) and the actuator duty cycle **(b)**.

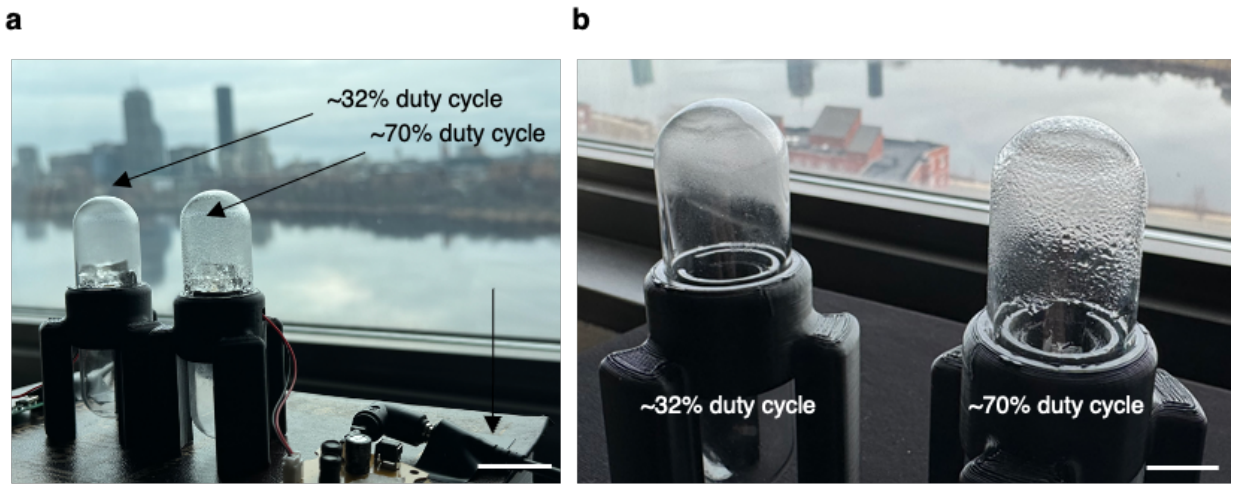

Supplementary Figure S32. A photograph of the ultrasonic actuator system loaded with HG-C specimens. a. Moisture release can be controlled by modulating the duty cycle from low (~32%) to high (~70%) as a function of time. **b**. A close view of the condensed water particles collected inside the two ultrasonic actuator systems. Scale bars: 16 cm (a); 8 cm (b).

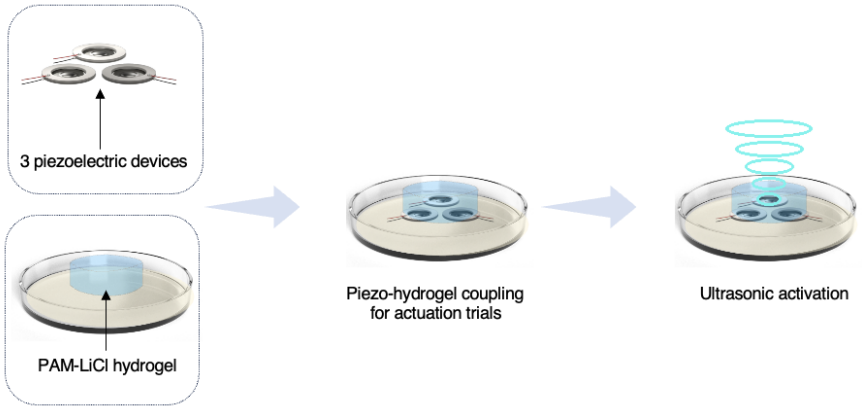

Supplementary Figure S33: Desorption test of HG-A hydrogel specimens employing three individual piezoelectric ultrasound devices together.

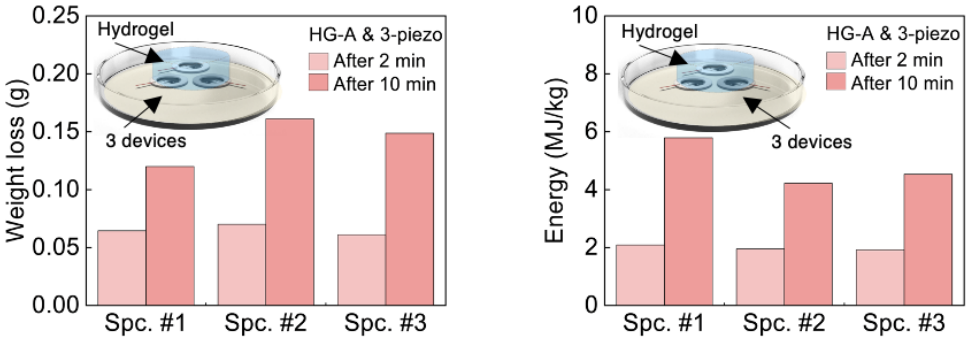

Supplementary Figure S34: Desorption behaviour of HG-A hydrogel (~2.6 g per specimen) under the actuation of three individual piezoelectric ultrasound devices for 10 minutes at 25% duty cycle. The weight loss (left) and corresponding energy consumption (right) of the specimens (~2.6 g per specimen) after 2 and 10 min, respectively.

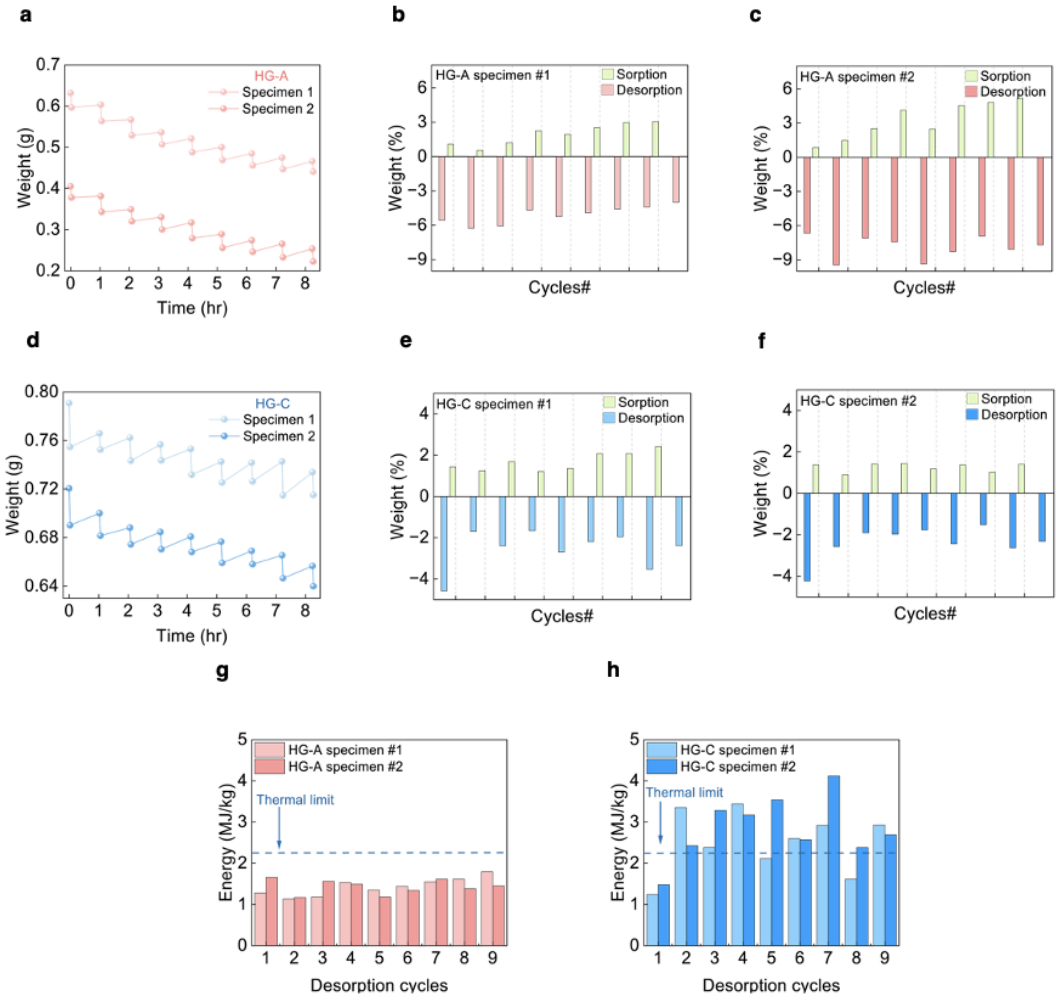

Supplementary Figure S35: Repeatability and energy efficiency of the proposed system using smaller HG-A specimens (≤16 mm diameter) for atmospheric water sorption and desorption with the energy consumption below the thermal limit for both HG-A (a-c, g) and HG-C (d-f, h).

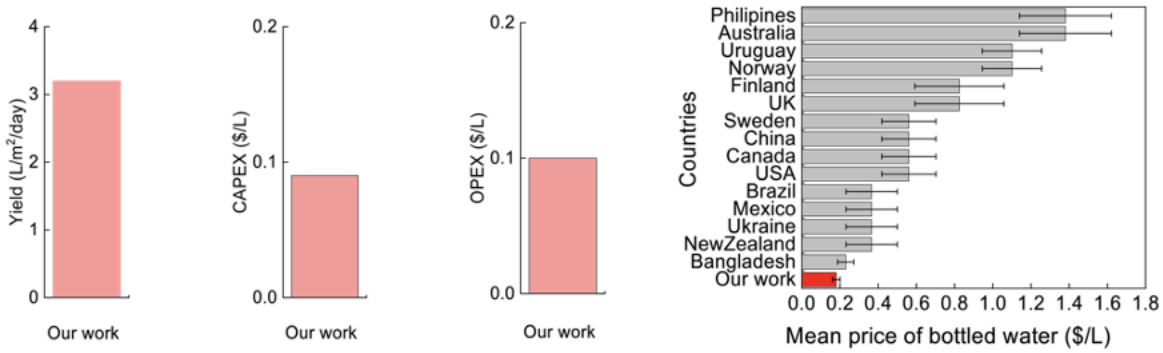

Supplementary Figure S36: A summary of the parameters (productivity, OPEX, and CAPEX) used in our techno-economic analysis to estimate the price of water ($/L) and a comparative study of mean price of bottled water among the countries.

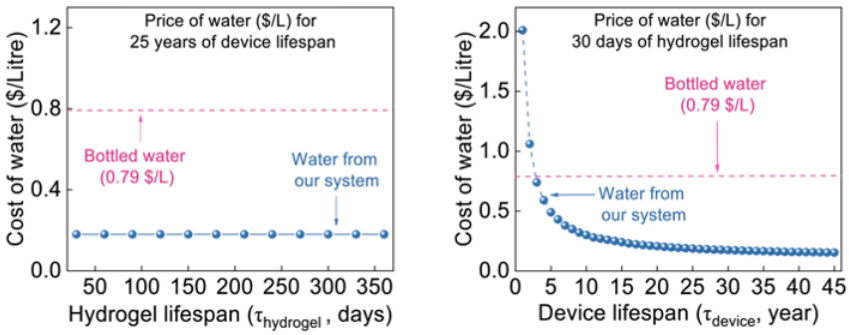

Supplementary Figure S37: Estimated cost of water as a function of hydrogel (a) and device (b) lifetime.

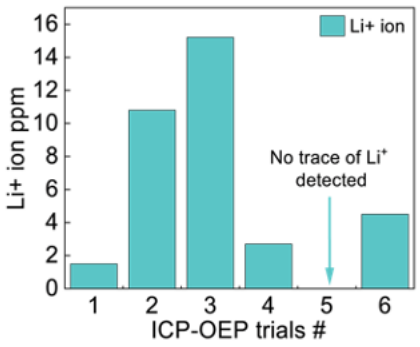

Supplementary Figure S38: Inductively coupled plasma optical emission spectrometry (ICP-OES) elemental analysis of the lithium-ion content in extracted water after sorption at 20% RH.

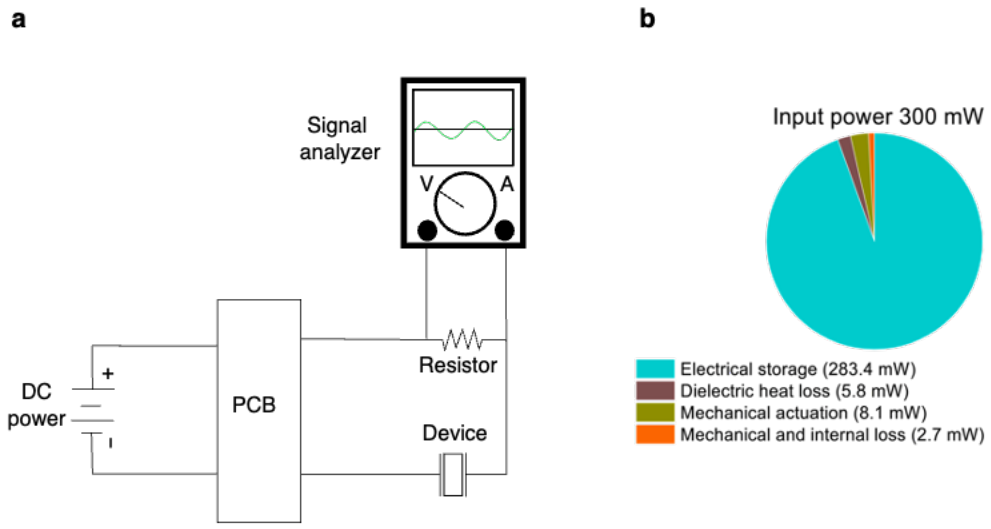

Supplementary Figure S39: Circuit diagram (**a**) used to characterize the input power fed to the piezoelectric transducer and a rough estimate of the power breakdown spent on thermal and mechanical actuation (**b**).

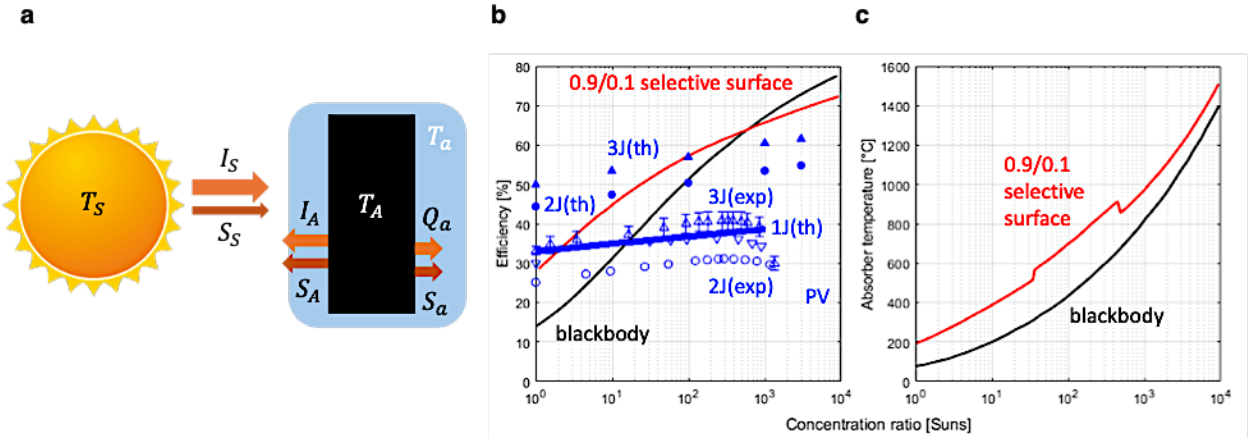

Supplementary Figure S40: (a) A schematic of a solar-thermal energy converter with the energy and entropy fluxes illustrated. (b) The limiting efficiency of solar thermal energy converters with a blackbody (black solid line) and a spectrally selective (red solid line) absorber as a function of solar concentration. The converted are assumed to operate at the Carnot efficiency. For spectrally selective absorbers, the transition frequency between high and low solar/infrared emittance levels (labeled as ratios α/ε) is optimized for each concentration ratio[24]. b. The corresponding equilibrium temperature of the solar-thermal absorbers with the optimized spectral transition point between high and low emittance levels as a function of solar concentration. Blue markers on panel (a) represent energy efficiency of PV cells[31–35]. Solid markers represent theoretical predictions (squares: a single-junction cell, circles: a dual-junction cell, triangles: a triple junction cell). Hollow markers correspond to the experimental data (circles: dual-junction, triangles: triple junction cells).

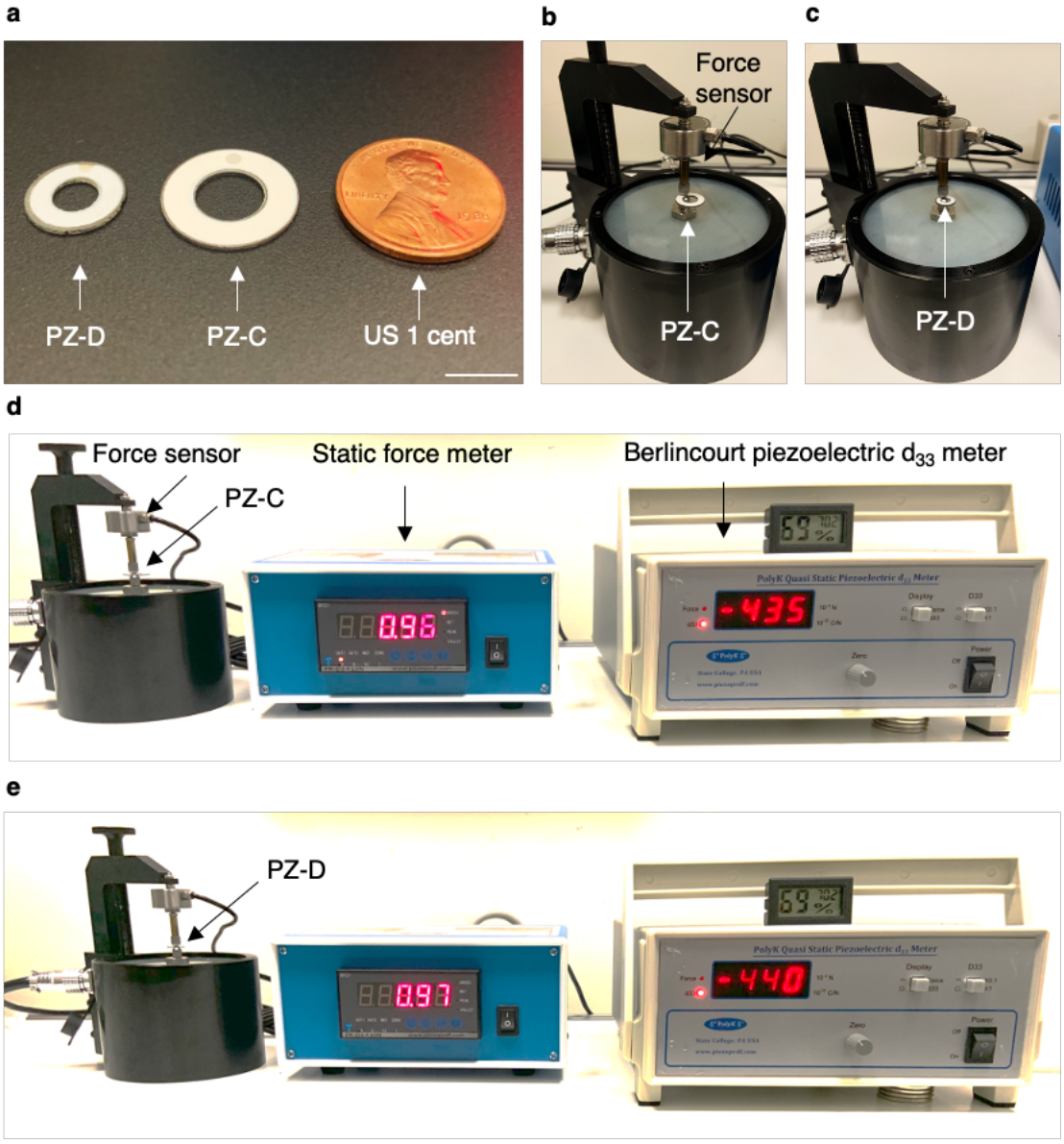

Supplementary Figure S41: Piezoelectric coefficient test setup in an ambient environment using a Berlincourt d_{33} (pC/N) meter. a Photo of PZ-C and PZ-D piezoelectric polycrystalline ceramics used in the ultrasonic transducer devices. **b, d** Characterizing the piezoelectric constant of PZ-C ($|d_{33}|$ = 435 pC/N) and **c, e** PZ-D ($|d_{33}|$ = 440 pC/N) actuator devices. The tests were conducted at a constant static force of ~1N as depicted in the photos at room temperature. Scale bar, 8 mm **(a).**

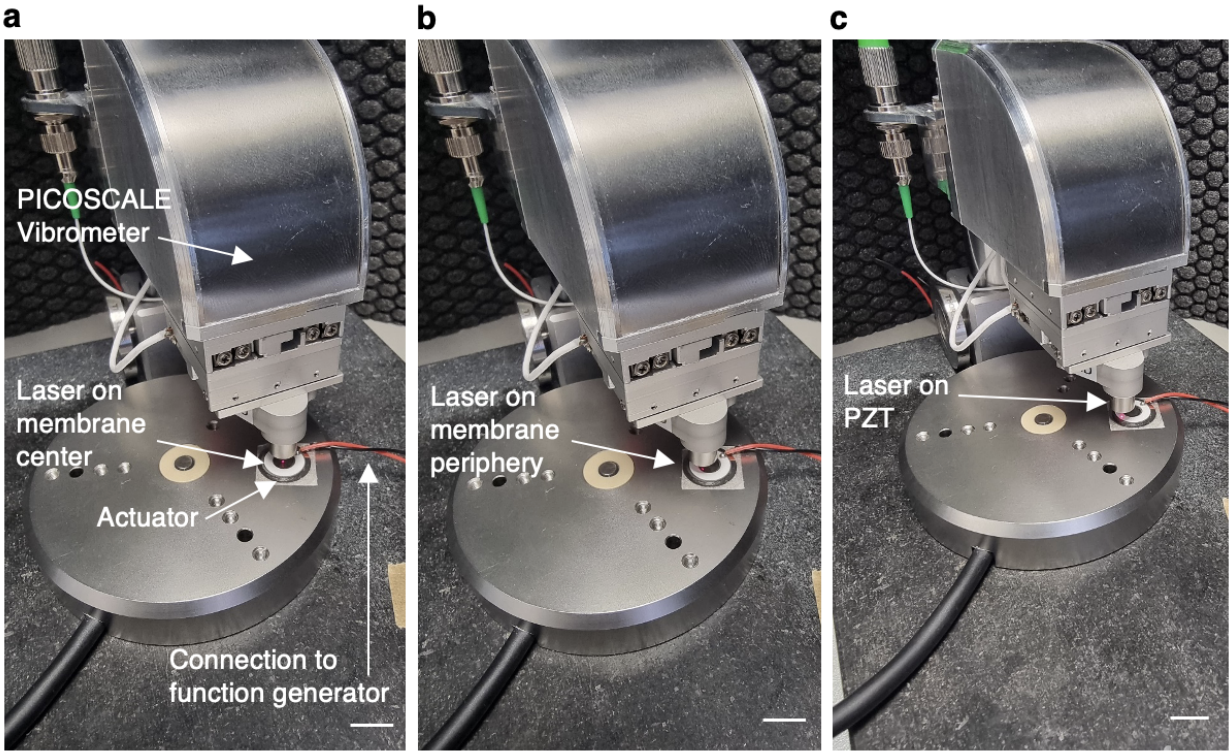

Supplementary Figure S42: Vibration deflection analysis using a PICOSCALE vibrometer. Laser beam focused on **a** the center of the mesh (M) and **b** a periphery (P) of the membrane. **c** Laser beam focused on the piezoelectric crystal. Scale bar, 16 mm **(a-c).**

References

1. Shuvo, I. I. Microfabrication and characterization of a new box-shaped high frequency (7.5 MHz) low aperture 2D phased ultrasound transducer array [Master's thesis]. (2023).
2. Shekhani, H. N. Characterization of the high power properties of piezoelectric ceramics using the burst method: methodology, analysis, and experimental approach. (2016). at <https://etda.libraries.psu.edu/files/final_submissions/11952>
3. IEEE. IEEE Standard on Piezoelectricity. *IEEE* (1987). doi:https://doi.org/10.1109/IEEESTD.1988.79638
4. J. Rojas & J. Morales. Design and Simulation of a Piezoelectric Actuated Valveless Micropump. *COMSOL Conf. Bost.* (2015). at <https://www.comsol.com/paper/design-and-simulation-of-a-piezoelectric-actuated-valveless-micropump-24671>
5. COMSOL. Eigenmodes of a Viscoelastic Structural Damper. *COMSOL* (2023). at <https://doc.comsol.com/5.5/doc/com.comsol.help.sme/sme_ug_modeling.05.004.html>
6. Toepke, M. W. & Murphy, W. L. in (ed. Ducheyne, P. B. T.-C. B.) 577–594 (Elsevier, 2011). doi:https://doi.org/10.1016/B978-0-08-055294-1.00045-3
7. Shamsipur, M., Taherpour, A. A. & Pashabadi, A. Comprehensive facilitating of water oxidation reaction by ultrasonic attenuation of hydrogen-bonded structure of water. *Ultrason. Sonochem.* **42,** 381–389 (2018).
8. Venegas-Sanchez, J. A., Tagaya, M. & Kobayashi, T. Effect of ultrasound on the aqueous viscosity of several water-soluble polymers. *Polym. J.* **45,** 1224–1233 (2013).
9. Sekine, Y., Takagi, H., Sudo, S., Kajiwara, Y., Fukazawa, H. & Ikeda-Fukazawa, T. Dependence of structure of polymer side chain on water structure in hydrogels. *Polymer (Guildf).* **55,** 6320–6324 (2014).
10. Wilson, C. T., Cha, H., Zhong, Y., Li, A. C., Lin, E. & El Fil, B. Design considerations for next-generation sorbent-based atmospheric water-harvesting devices. *Device* **1,** 100052 (2023).
11. Zhong, Y., Zhang, L., Li, X., El Fil, B., Díaz-Marín, C. D., Li, A. C., Liu, X., LaPotin, A. & Wang, E. N. Bridging materials innovations to sorption-based atmospheric water harvesting devices. *Nat. Rev. Mater.* **9,** 681–698 (2024).
12. Conde, M. R. Properties of aqueous solutions of lithium and calcium chlorides: formulations for use in air conditioning equipment design. *Int. J. Therm. Sci.* **43,** 367–382 (2004).
13. Moussa, R. R. The Effect of Piezo-Bumps on Energy Generation and Reduction of the Global Carbon Emissions. in *WSEAS Trans. Environ. Dev.* (WSEAS, 2019). at <https://wseas.com/journals/articles.php?id=1976>
14. PI Ceramic. *Reliability & Lifetime of Multilayer Piezo Actuators*. (2025). at <https://www.pi-usa.us/fileadmin/user_upload/pi_us/files/catalogs/Piezo_Actuator_Lifetime_Test_Reliability_Results.pdf>
15. US Bureau of Labor Statistics. Average Energy Prices, Boston-Cambridge-Newton — December 2024. *News Release* (2024). at <https://www.bls.gov/regions/northeast/news-release/averageenergyprices_boston.htm>
16. Statista. How Much Does a Bottle of Water Cost? *Bottled water Mark. Worldw.* (2023).
17. Adeel, M., Zain, M., Shakoor, N., Ahmad, M. A., Azeem, I., Aziz, M. A., Tulcan, R. X. S.,

Rathore, A., Tahir, M., Horton, R., Xu, M. & Yukui, R. Global navigation of Lithium in water bodies and emerging human health crisis. *npj Clean Water* **6,** 33 (2023).
18. Iordache, A. M., Voica, C., Roba, C. & Nechita, C. Lithium Content and Its Nutritional Beneficence, Dietary Intake, and Impact on Human Health in Edibles from the Romanian Market. *Foods* **13,** 592 (2024).
19. Szklarska, D. & Rzymski, P. Is Lithium a Micronutrient? From Biological Activity and Epidemiological Observation to Food Fortification. *Biol. Trace Elem. Res.* **189,** 18–27 (2019).
20. Schrauzer, G. N. Lithium: Occurrence, Dietary Intakes, Nutritional Essentiality. *J. Am. Coll. Nutr.* **21,** 14–21 (2002).
21. KRACHLER, M. & SHOTYK, W. Trace and ultratrace metals in bottled waters: Survey of sources worldwide and comparison with refillable metal bottles. *Sci. Total Environ.* **407,** 1089–1096 (2009).
22. Bilgen, O., Amin Karami, M., Inman, D. J. & Friswell, M. I. The actuation characterization of cantilevered unimorph beams with single crystal piezoelectric materials. *Smart Mater. Struct.* **20,** 055024 (2011).
23. Fuji Ceramics. PZT Material Selection Guide. *Fuji Ceram. Corp.* (2022). at <https://www.fujicera.co.jp/en/feature/4164/>
24. Boriskina, S. V., Tong, J. K., Hsu, W.-C., Liao, B., Huang, Y., Chiloyan, V. & Chen, G. Heat meets light on the nanoscale. *Nanophotonics* **5,** 134–160 (2016).
25. Boriskina, S. V, Green, M. A., Catchpole, K., Yablonovitch, E., Beard, M. C., Okada, Y., Lany, S., Gershon, T., Zakutayev, A., Tahersima, M. H., Sorger, V. J., Naughton, M. J., Kempa, K., Dagenais, M., Yao, Y., Xu, L., Sheng, X., Bronstein, N. D., Rogers, J. A., Alivisatos, A. P., Nuzzo, R. G., Gordon, J. M., Wu, D. M., Wisser, M. D., Salleo, A., Dionne, J., Bermel, P., Greffet, J.-J., Celanovic, I., Soljacic, M., Manor, A., Rotschild, C., Raman, A., Zhu, L., Fan, S. & Chen, G. Roadmap on optical energy conversion. *J. Opt.* **18,** 073004 (2016).
26. Badescu, V. Spectrally and angularly selective photothermal and photovoltaic converters under one-sun illumination. *J. Phys. D. Appl. Phys.* **38,** 2166–2172 (2005).
27. McEnaney, K., Kraemer, D. & Chen, G. DIRECT HEAT-TO-ELECTRICITY CONVERSION OF SOLAR ENERGY. *Annu. Rev. Heat Transf.* **15,** 179–230 (2012).
28. Peter Bermel, Jeongwon Lee, John D. Joannopoulos, Ivan Celanovic, M. S. in *Annu. Rev. Heat Transf.* (Begell House, Inc, 2012). at <https://web.ics.purdue.edu/~pbermel/pdf/Bermel12.pdf>
29. Yeng, Y. X., Ghebrebrhan, M., Bermel, P., Chan, W. R., Joannopoulos, J. D., Soljačić, M. & Celanovic, I. Enabling high-temperature nanophotonics for energy applications. *Proc. Natl. Acad. Sci.* **109,** 2280–2285 (2012).
30. McEnaney, K. Modeling of Solar Thermal Selective Surfaces and Thermoelectric Generators. (2010). at <https://dspace.mit.edu/bitstream/handle/1721.1/65308/745771158-MIT.pdf%3Bjsessionid%3D3EF48C7AA6B0F88E3864BF0F1D5ECDD7?sequence%3D2>
31. Ekins-Daukes, N. J., Soeriyadi, A., Zhao, W., Bremner, S. & Pusch, A. Loss analysis for single junction concentrator solar cells. *AIP Conf. Proc.* **2012,** 40003 (2018).
32. Micha, D. N. & Silvares Junior, R. T. The Influence of Solar Spectrum and Concentration Factor on the Material Choice and the Efficiency of Multijunction Solar Cells. *Sci. Rep.* **9,**

20055 (2019).
33. Siefer, G., Baur, C., Meusel, M., Dimroth, F., Bett, A. W. & Warta, W. Influence of the simulator spectrum on the calibration of multi-junction solar cells under concentration. in *Conf. Rec. Twenty-Ninth IEEE Photovolt. Spec. Conf. 2002.* 836–839 (2002). doi:10.1109/PVSC.2002.1190709
34. Fernández, E. F., Siefer, G., Schachtner, M., García Loureiro, A. J. & Pérez-Higueras, P. Temperature coefficients of monolithic III-V triple-junction solar cells under different spectra and irradiance levels. *AIP Conf. Proc.* **1477,** 189–193 (2012).
35. Geisz, J. F., Friedman, D. J., Ward, J. S., Duda, A., Olavarria, W. J., Moriarty, T. E., Kiehl, J. T., Romero, M. J., Norman, A. G. & Jones, K. M. 40.8% efficient inverted triple-junction solar cell with two independently metamorphic junctions. *Appl. Phys. Lett.* **93,** 123505 (2008).
36. LaPotin, A., Zhong, Y., Zhang, L., Zhao, L., Leroy, A., Kim, H., Rao, S. R. & Wang, E. N. Dual-Stage Atmospheric Water Harvesting Device for Scalable Solar-Driven Water Production. *Joule* **5,** 166–182 (2021).
37. Hanikel, N., Prévot, M. S., Fathieh, F., Kapustin, E. A., Lyu, H., Wang, H., Diercks, N. J., Glover, T. G. & Yaghi, O. M. Rapid Cycling and Exceptional Yield in a Metal-Organic Framework Water Harvester. *ACS Cent. Sci.* **5,** 1699–1706 (2019).
38. Xu, J., Li, T., Yan, T., Wu, S., Wu, M., Chao, J., Huo, X., Wang, P. & Wang, R. Ultrahigh solar-driven atmospheric water production enabled by scalable rapid-cycling water harvester with vertically aligned nanocomposite sorbent. *Energy Environ. Sci.* **14,** 5979–5994 (2021).
39. Shan, H., Li, C., Chen, Z., Ying, W., Poredoš, P., Ye, Z., Pan, Q., Wang, J. & Wang, R. Exceptional water production yield enabled by batch-processed portable water harvester in semi-arid climate. *Nat. Commun.* **13,** 5406 (2022).
40. Almassad, H. A., Abaza, R. I., Siwwan, L., Al-Maythalony, B. & Cordova, K. E. Environmentally adaptive MOF-based device enables continuous self-optimizing atmospheric water harvesting. *Nat. Commun.* **13,** 4873 (2022).
41. Qi, H., Wei, T., Zhao, W., Zhu, B., Liu, G., Wang, P., Lin, Z., Wang, X., Li, X., Zhang, X. & Zhu, J. An Interfacial Solar-Driven Atmospheric Water Generator Based on a Liquid Sorbent with Simultaneous Adsorption–Desorption. *Adv. Mater.* **31,** (2019).
42. Wang, J. Y., Liu, J. Y., Wang, R. Z. & Wang, L. W. Experimental investigation on two solar-driven sorption based devices to extract fresh water from atmosphere. *Appl. Therm. Eng.* **127,** 1608–1616 (2017).
43. Fathieh, F., Kalmutzki, M. J., Kapustin, E. A., Waller, P. J., Yang, J. & Yaghi, O. M. Practical water production from desert air. *Sci. Adv.* **4,** (2018).
44. Kim, H., Rao, S. R., Kapustin, E. A., Zhao, L., Yang, S., Yaghi, O. M. & Wang, E. N. Adsorption-based atmospheric water harvesting device for arid climates. *Nat. Commun.* **9,** 1191 (2018).
45. Xu, J., Li, T., Chao, J., Wu, S., Yan, T., Li, W., Cao, B. & Wang, R. Efficient Solar-Driven Water Harvesting from Arid Air with Metal–Organic Frameworks Modified by Hygroscopic Salt. *Angew. Chemie Int. Ed.* **59,** 5202–5210 (2020).
46. Li, R., Shi, Y., Wu, M., Hong, S. & Wang, P. Improving atmospheric water production yield: Enabling multiple water harvesting cycles with nano sorbent. *Nano Energy* **67,** 104255 (2020).
47. Xu, J., Li, T., Yan, T., Wu, S., Wu, M., Chao, J., Huo, X., Wang, P. & Wang, R. Ultrahigh solar-

driven atmospheric water production enabled by scalable rapid-cycling water harvester with vertically aligned nanocomposite sorbent. *Energy Environ. Sci.* **14,** 5979–5994 (2021).
48. Xu, J., Huo, X., Yan, T., Wang, P., Bai, Z., Chao, J., Yang, R., Wang, R. & Li, T. All-in-one hybrid atmospheric water harvesting for all-day water production by natural sunlight and radiative cooling. *Energy Environ. Sci.* **17,** 4988–5001 (2024).
49. Yang, X., Chen, Z., Xiang, C., Shan, H. & Wang, R. Enhanced continuous atmospheric water harvesting with scalable hygroscopic gel driven by natural sunlight and wind. *Nat. Commun.* **15,** 7678 (2024).
50. High Purity Lithium Chloride 99% Cas 7447-41-8 - Buy Lithium Chloride cas 7447-41-8 welding Agent Product on Alibaba.com. *Alibaba.com* (2024). at <https://www.alibaba.com/product-detail/High-Purity-Lithium-Chloride-99-CAS_1600991631465.html>
51. Shandong Up Chemical Technology. China Factory Price Acrylamide 98%Acrylamide. *Alibaba.com* (2024). at <https://www.alibaba.com/product-detail/China-factory-price-Acrylamide-98-Acrylamide_1600137018371.html>
52. Nanjing Jiayi Sunway Chemical Ltd. Ammonium Persulfate (NH4)2S2O8 CAS 7727-54-0 Ammonium Persulfate 98.66%. *Alibaba.com* (2024). at <https://www.alibaba.com/product-detail/Ammonium-Persulfate-NH4-2S2O8-CAS-7727_1601015455421.html>
53. Qingdao Jinyu Chemical. NN-Methylenebisacrylamide MBA Methylene Bisacrylamide CAS 110-26-9. *Alibaba.com* (2024). at <https://www.alibaba.com/product-detail/factory-direct-supply-N-N-Methylenebisacrylamide_1600882499349.html>
54. Sigma. N,N,N′,N′-Tetramethylethylenediamine (≥99.5%, purified by redistillation). *Sigma-Aldrich Chem. Build. Blocks* (2024). at <https://www.sigmaaldrich.com/US/en/product/aldrich/411019>
55. N,N,N’,N’-tetramethylethylenediamine With Low Price Cas 110-18-9 - Buy Tmeda,Cas 110-18-9 Tmeda. *Alibaba.com* (2024). at <https://www.alibaba.com/product-detail/N-N-N-N-Tetramethylethylenediamine-with_1600272967916.html>
56. Dongguan Cosson Electronic Plastic Ltd. 16mm Ultrasonic Mist Maker with Small Driver Circuit. *Alibaba.com* (2025). at <https://www.alibaba.com/product-detail/16mm-Ultrasonic-Mist-Maker-with-Small_60392165208.html?spm=a2700.details.you_may_like.1.7b8f2d7fBLILGw>
57. U.S. Energy Information Administration. Average Price of Electricity to Ultimate Customers. *Electr. Power Mon.* (2025). at <https://www.eia.gov/electricity/monthly/epm_table_grapher.php?t=epmt_5_3>
58. COMSOL Multiphysics® v. 6.1. www.comsol.com. COMSOL AB, Stockholm, Sweden.